GeoStorage

Vol. 2, No. 3, p. 274-296, 2026

Research article

Aquifer Thermal Energy Storage for Intermittent Renewable Energy: Thermo-Hydraulic Controls and a Dual-Zone Heat Transfer Mechanism

Yongxiang Zheng[1,2,3], Jie Fan[1], Wei Yuan[3], Qinghe Niu[1], Songhua Shang[1], Fengting Xu[1*]

[1] *School of Civil Engineering, Shijiazhuang Tiedao University, Shijiazhuang, 050043, China*
[2] *Hebei Technology and innovation Center on Safe and Efficient Mining of Metal Mine, Shijiazhuang, 050043, China*
[3] *Xiong'an Research Institute for Underground Space and Deep Resources Utilization and Development, Shijiazhuang Tiedao University, Shijiazhuang, 050043, China*

Keywords:
Aquifer thermal energy storage (ATES)
intermittent renewable energy
thermo-hydraulic coupling
thermal stabilization
convective heat transfer
thermal response

Cited as:
Zheng YX, Fan J, Yuan W, et al. 2026. Aquifer Thermal Energy Storage for Intermittent Renewable Energy: Thermo-Hydraulic Controls and a Dual-Zone Heat Transfer Mechanism. *GeoStorage*, 2(3), 274-296.
https://doi.org/10.46690/gs.2026.03.06

Abstract:
Aquifer thermal energy storage (ATES) provides a promising subsurface pathway for integrating intermittent renewable energy by converting fluctuating thermal inputs into a more stable energy output. This study develops an ATES-based energy storage concept for the integration of solar energy, wind-derived electricity, and industrial waste heat, and investigates its thermo-hydraulic response under periodically fluctuating heat injection. A three-dimensional reservoir model was established using CMG STARS to characterize the spatiotemporal evolution of formation and production temperatures and to evaluate the effects of injection temperature, injection-production pressure difference, permeability, porosity, rock volumetric heat capacity, and thermal conductivity. The results show that temperature fluctuations are progressively attenuated during subsurface transport, demonstrating the capacity of the aquifer to buffer intermittent thermal inputs. Production temperature increases with injection temperature, pressure difference, and permeability, but decreases with increasing rock thermal conductivity, whereas porosity and volumetric heat capacity exert comparatively limited effects. Thermal response time is governed primarily by fluid transport and is shortened by higher permeability and larger injection-production pressure differences. Mechanistically, convective heat transport dominates thermal propagation between the injection and production wells, while conductive heat transfer controls energy dissipation toward the surrounding formation. Based on these characteristics, a dual-zone heat transfer mechanism consisting of a flow-dominated convective zone and a conduction-dominated peripheral zone is proposed to explain thermal stabilization and heat loss within the reservoir. These findings clarify the thermo-hydraulic controls on ATES performance under fluctuating energy input and provide a mechanistic basis for using subsurface aquifers to support the integration and stabilization of intermittent renewable energy.

1 Introduction

The structural reduction in fossil fuel usage and deployment of integrated multi-energy complementary systems constitute dual core strategies for achieving low carbon goals. Currently, geothermal, solar, and wind energy dominate renewable deployment, while industrial waste heat recovery represents a substantial untapped potential. However, these sources exhibit fundamental constraints: wind power's inherent intermittency induces grid instability; solar energy availability fluctuates diurnally and seasonally (Guo et al., 2021); geothermal extraction rates are constrained by reservoir longevity (Han et al., 2024). To address these barriers, a pivotal research challenge emerges: developing thermo-hydraulic coupling models to convert intermittent renewables into stable supply through multi-energy

* Corresponding author.
E-mail address: zhengyx@stdu.edu.cn (Zheng YX); fj13616159755@163.com (Fan J); yuanweisuper001@126.com (Yuan W); qinghniu@163.com (Niu QH); shangsh@stdu.edu.cn (Shang SH); xufengting1234@126.com (Xu FT)

Received Aug. 28, 2026; revised Sep. 9, 2026; accepted Sep. 14, 2026; available online Sep. 20, 2026.

Yandy Scientific Press

storage and conversion (Brown et al., 2024).

Energy storage technology provides a technical framework for energy conversion. Among them, geotechnical energy storage has attracted research interest due to its compact space requirements and high storage capacity. Current underground storage facilities—including tunnels, pools, mines, caverns, and aquifers—can accommodate significant volumes of fluctuating energy (Dahash et al., 2019; Novo et al., 2010). Among these, aquifer thermal energy storage (ATES) offers optimal heat storage efficiency. ATES operates in two modes: medium-low temperature (MLT) and high temperature (HT). MLT-ATES utilizes shallow aquifer layers at approximately 30℃ for seasonal energy storage, implementing a cyclic process where heat is stored via hot water injection in summer and recovered through water extraction in winter (Pellegrini et al., 2019). HT-ATES employs deep geothermal reservoirs exceeding 50℃. It has advantages such as large spatial capacity, high temperature, and good thermal insulation performance, making them safer and space saving compared to other energy storage methods. Additionally, HT-ATES enables synergistic utilization of existing geothermal resources, providing a distinct operational advantage.

ATES has been extensively studied through theoretical and field investigations, with heat extraction quantity and recovery efficiency identified as critical performance factors (Wang et al., 2024; Zhou et al., 2024; Heldt et al., 2024). It is essential to understand the temporal and spatial evolution of temperature within the formations. Heldt et al. (2024, 2021) conducted high-temperature ATES injection experiments and simulations using field geological data to analyze the influence of hydraulic and thermodynamic parameter on heat recovery and formation temperature. Wang et al. (2024) conducted uncertainty analysis to evaluated the effect of fracture aperture, permeability, injection rate, and injection temperature on thermal breakthrough time and total heat recovery. Huang et al. (2021) focus on the total heat and recovery rate by analysis of heat flow and loss. Zhou et al. (2024) examined the effects of viscosity differences and volumetric heat capacity variations between CO_2 and water on fluid flow behavior and production temperature stability. Gao et al. (2019) established a well-to-well model to analyze the uncertainty effects of injection temperature, well spacing, aquifer thickness, permeability, and hydraulic gradient on heat recovery efficiency. Bloemendal et al. (2018) analyzed 331 samples to determine the effects of flow rate, reservoir radius, and formation thermal conductivity on heat recovery rate. In summary, physical properties (permeability, porosity), thermodynamic properties (volumetric heat capacity, thermal conductivity), production parameters (pressure gradient, working medium), and other factors primarily govern heat production and heat recovery rate.

ATES enables thermal energy storage and balancing, facilitating efficient seasonal energy utilization via high-temperature aquifer storage and extraction cycles. Kastner et al. (2017) investigated ATES availability for seasonal solar thermal storage within Jurassic sandstone formations in northeastern Germany. Kastner et al. (2017) analyzed ATES feasibility for direct cooling, heat pump cooling/heating, and solar collector heating systems in Tehran, Iran. Pellegrini et al. (2019) established six EU-based ATES pilot projects. Bu et al. (2022) proposed solar energy storage in shallow reservoirs using abandoned oil/gas fields and mines. These studies demonstrate solar energy storage in ATES enables combined energy utilization. Consequently, ATES-based multi-energy complementary systems can be developed, exemplified by Els et al. (2021) integrating geothermal, wind, electrical, and solar energy. Zhang et al. (2024) examined formation temperature evolution in a geothermal-based multi-energy complementary system in Xiong'an, China. Perera et al. (2023) developed a long-term model of heat storage incorporating distributed multi-energy systems with ATES. The above empirical studies demonstrate that ATES-based multi-energy complementary systems can achieve integrated utilization of diverse energy sources through synergistic coordination.

While existing ATES solutions effectively manage seasonal energy shifts, their inability to mitigate sub-daily renewable intermittency and associated heat transport losses motivates our approach. We propose a novel aquifer-based system leveraging diurnal thermal cycling to continuously stabilize multi-energy inputs (solar/wind/industrial waste heat). The paper is structured as follows: Section 2 details the multi-energy complementary system design; Section 3 specifies the model and parameters; Section 4 simulates the temperature evolution of formation and production well; Section 5 analyzes sensitivity of hydraulic/permeability parameters on temperature evolution; Section 6 proposes a dual-zone well configuration comprising convective zone and peripheral zone for thermal front control. This study provides theoretical guidance for the design of multi-energy complementary systems and geothermal exploitation.

2 Introduction to ATES-based multi-energy complementary system

The multi-energy complementary energy storage system comprises three modules: the energy collection module, the balancing and conversion module, and the utilization module (shown in Fig.1). Fluctuating high-temperature thermal energy is obtained from solar thermal, wind energy, and industrial waste heat sources. Utilizing an aquifer geothermal reservoir as thermal storage, this thermal energy is balanced and converted into a stable supply of high-temperature water. Finally, the heat drives geothermal power generation and supports various downstream applications.

2.1 Energy collection module

The energy collection module harvests thermal energy from solar thermal collectors, industrial waste heat recovery, electricity conversion form solar and wind energy, tailored to site-specific conditions. While solar and wind energy constitute renewable sources, their inherent intermittency and irregular power output pose operational challenges. Industrial waste heat recovery can enhance energy utilization rates. However, its typically low-grade thermal characteristics complicate cascaded utilization. This module integrates fluctuating energy inputs, which are transferred via heat exchangers into the injection pipeline system. The process delivers stabilized fluctuating thermal energy (e.g., high-temperature water or alternative media) to the injection system at consistent mass flow rates.

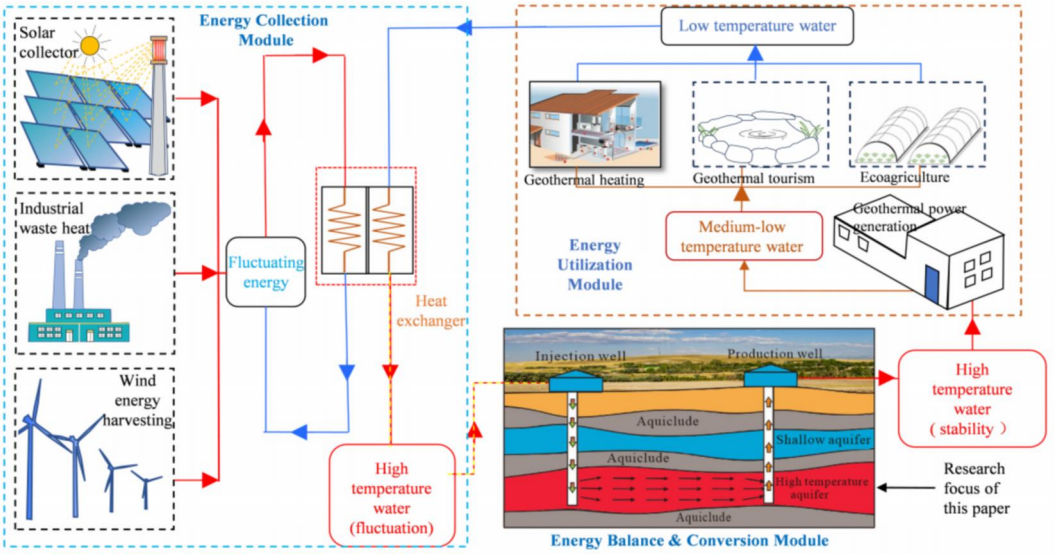

Fig. 1 ATES-based multi-energy complementary system

The specific details of this module are shown in Fig.2. The module includes two modes: heat exchange and electric heating. The heat exchange mode mainly utilizes industrial waste heat and solar energy collection to heat the working fluid, which is then heat-exchanged with used cold water through a plate heat exchanger. The electric heating mode heats the working fluid through wind power, photovoltaic power, and grid power to produce high-temperature fluid. The main sources of electric energy are photovoltaic power and wind power. The utilization of grid power includes supplementing the shortage of wind and solar power and utilizing grid off-peak power. The addition of grid power ensures the stability of system operation. It should be mentioned that in this scenario, it is not necessary to choose all options; only the appropriate module and energy source should be selected according to site conditions to maximize efficiency.

2.2 Energy balance and conversion module

The energy balance and conversion module are based on the geothermal reservoir. Because of the effective heat retention and accumulation mechanisms of geothermal reservoir, it can guarantee the effective recovery of injected energy. The geothermal system fulfills the role of energy balance transformation in the system after the fluctuating high-temperature water enters the formation, ultimately obtaining a steady heat flow through the production well. Consequently, an energy “power bank” (energy supply and energy storage) replaces the single energy “battery” (energy supply) in this system. This research specifically investigates thermal evolution dynamics during diurnally fluctuating injection regimes influenced by solar intermittency, where injected water alternates between high-temperature conditions (daytime) and medium-temperature conditions (nighttime, still exceeding formation temperatures), implementing a 12-hour high-temperature injection/12-hour medium-temperature injection cyclical protocol.

2.3 Energy utilization module

The energy utilization module converts the stable high-temperature water produced by the energy balance conversion module into electricity through the power generation. This allows the system to convert intermittent solar and wind energy as well as low-quality industrial waste heat into steady electricity energy output. To increase the effectiveness of heat energy utilization, the residual heat after electricity generation can be utilized for heating, tourism, eco-agriculture.

The specific details of this module are shown in Fig.3. The energy utilization module encompasses both a power generation mode and a secondary utilization mode. For the power generation mode, the geothermal power generation system chosen is a flash-binary working fluid power generation system. The high-temperature water produced by the production well enters the flash evaporator (with an internal pressure lower than the saturation pressure of the geothermal water), where the water undergoes pressure reduction and flash evaporation, and the resulting low-pressure steam is sent to the steam turbine for expansion and power generation. The resulting saturated water continues to enter the low-boiling point organic working fluid power generation system. In this system, the low-boiling point organic working fluid is heated by an evaporator to drive the generator for power generation. After power generation, the temperature of the geothermal water decreases, but it can still be applied to scenarios such as geothermal heating, geothermal tourism, and geothermal agriculture according to the on-site conditions. To minimize the impact of the re-injected water on the aquifer, a heat exchanger is used to complete the temperature exchange between the produced water and the usage water.

This system overcomes critical limitations—low-grade industrial waste heat utilization barriers, geothermal reservoir longevity constraints, and solar/wind intermittency—through synergistic integration of wind, solar, geothermal, and waste heat resources. By enabling full utilization of clean energy, it achieves core decarbonization objectives. Crucially, Whether

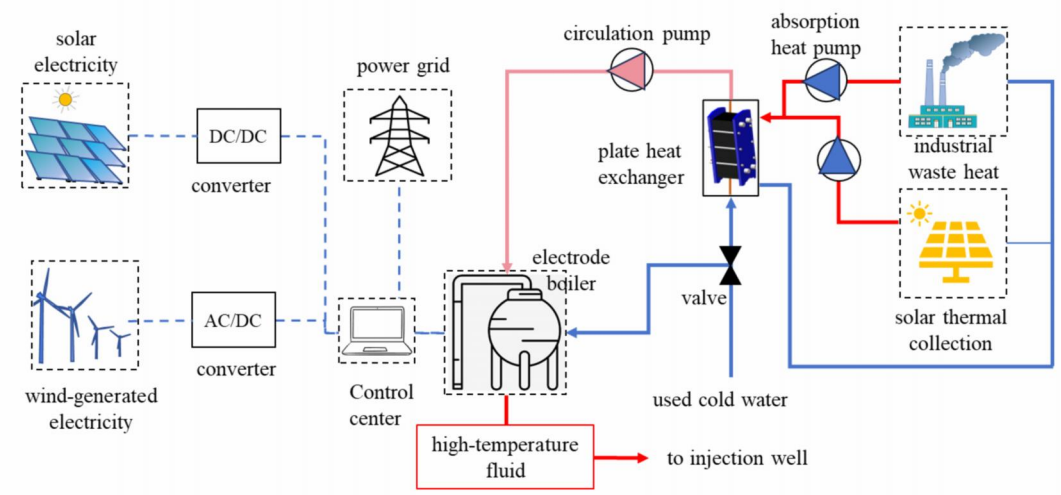

Fig. 2 Workflow of energy collection module

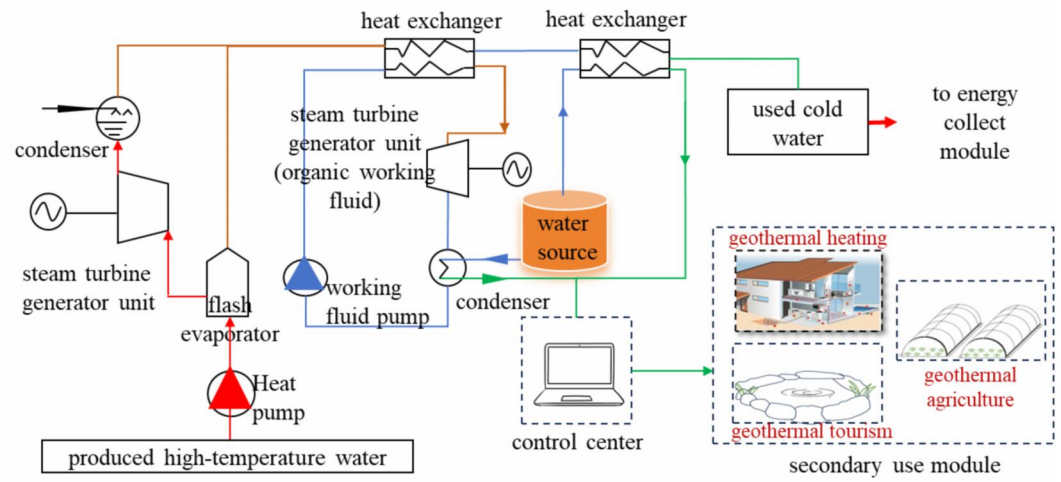

Fig. 3 Workflow of energy utilization module

the aquifer geothermal reservoir can achieve balanced temperature conversion is the main problem with this system. As a result, the evolution law and mechanism influencing the temperature of formation and water production will be thoroughly examined in this work.

3 Model and parameters

3.1 Mathematic model

The governing equations are governed by the following fundamental assumptions:

(1) Single-phase fluid flow without phase transitions occurs within the aquifer reservoir.
(2) Fluid flow through porous media obeys Darcy's law.
(3) Instant thermal equilibrium exists between the rock matrix and pore fluid.

The macroscopic mass conservation in porous media is described by the continuity equation:

$$\frac{\partial(\varphi\rho)}{\partial t} + \nabla \cdot (\rho(u) = 0 \tag{1}$$

where,φ is the porosity, ρ is the density of the fluid, and u is the apparent velocity of fluid. The fluid flow is described by Darcy's law, as follows

$$u = -\frac{k}{\mu}\nabla p \tag{2}$$

where, k is the permeability, μ is the viscosity of fluid, and p is the pressure.

Assuming an isotropic porous medium under local thermal equilibrium conditions, the solid-phase energy balance equation derived from the First Law of Thermodynamics is given by:

$$\theta_s(\rho C_p)_s \frac{\partial T_s}{\partial t} = \theta_s \nabla \cdot (-\lambda_s \nabla T_s) + \theta_s Q_s \tag{3}$$

Similarly, for the fluid, there is

$$\theta_f \left(\rho C_p\right)_f \frac{\partial T_f}{\partial t} + \left(\rho C_p\right)_f u \cdot \nabla T_f = \theta_f \nabla \cdot \left(-\lambda_f \nabla T_f\right) + \theta_f Q_f \tag{4}$$

According to the local thermal equilibrium conditions, $T_s = T_f = T$. Therefore, the heat transfer equation can be obtained by combining Eq. 3 and Eq. 4 as follows:

$$(\rho C_p)_{\text{eff}} \frac{\partial T}{\partial t} + \rho_f C_{p,f} \boldsymbol{u} \cdot \nabla T + \nabla \cdot (-\lambda_{\text{eff}} \nabla T) = Q_{\text{eff}} \quad (5)$$

where, f and s represent fluid and solid respectively, ρ is density, C_p is the heat capacity under constant pressure, and θ_s is volume fraction of solids. Since the formation is an aquifer, the porous medium is completely saturated. And the fraction of fluid volume is equal to the porosity, that is, $\theta_f = \phi$, $\theta_s = 1 - \theta_f$.

The thermal properties of the fluid and porous medium are collectively defined as effective properties: apparent heat capacity, apparent thermal conductivity, and apparent heat generation rate, expressed as follows:

$$(\rho c_p)_{eff} = \theta_s \rho_s c_{p,s} + \theta_f \rho_f c_{p,f} \quad (6)$$

$$\lambda_{eff} = \theta_s \lambda_s + \theta_f \lambda_f \quad (7)$$

$$Q_{eff} = \theta_s Q_s + \theta_f Q_f \quad (8)$$

3.2 Numerical model and parameters

The geothermal system has a good mechanism of heat accumulation and insulation system, so this paper establishes a numerical model as shown in Fig.4. The model comprises three layers: a target aquifer formation bounded by upper and lower impermeable caprocks (Impermeable Layer I and II). Model dimensions are 150 m × 150 m × 14 m, with a 6 m thick aquifer sandwiched between two 4 m thick caprocks. The aquifer with a target layer in the model has good permeability, and the other two layers are aquifuge with low permeability.

The formations hosting geothermal aquifers predominantly comprise carbonate rocks, sandstones, and magmatic rocks. The determination of relevant parameters in this study is based on a layered sandstone aquifer model. The specific parameter values are provided in Table 1, with their selections justified according to Reference (Zhang et al., 2024; Roded et al., 2024; Mantei et al., 2025; Computer Modelling Group Ltd., 2014). Besides, the initial formation temperature is 70 ℃ and the formation pressure is 14 MPa. The software used in this research is CMG STARS. It is a thermal reservoir simulator capable of accurately modeling various thermal recovery processes, ranging from simple to highly complex. It is primarily applied in reservoir simulation and has also been widely utilized in geothermal development.

The model incorporates an injection well and a production well spaced 60 m apart. Both wells are exclusively perforated within the target aquifer formation. Constant-pressure boundaries are imposed: 16 MPa at the injection well and 11 MPa at the production well. To prevent excessive fluid rate, the production well operates under a maximum flow rate constraint of 500 m^3/d. When the flow rate exceeds this threshold, the well switches to constant-rate production mode.

The injection well receives thermal energy from three sources: solar thermal collectors, wind power conversion systems, and industrial waste heat recovery units. Accounting for solar intermittency, the injected water temperature follows a diurnal cyclic profile: 12-hour high-temperature injection (120°C) during daylight, transitioning to 12-hour medium-temperature injection (80°C) at night.

4 Temperature distribution and evolution of base case

4.1 Formation temperature distribution and evolution

The system's applicability critically depends on the aquifer's thermal balance capacity for fluctuating energy inputs. Fig.5 demonstrates formation temperature evolution at radial distances from the injection well, showing progressive temperature rise from the 70°C baseline upon high-temperature water injection. At 3 m, temperature fluctuations directly correlate with injection transients, while at 6m fluctuations persist with reduced amplitude. The 9m temperature profile exhibits predominantly stabilized behavior with minor fluctuations, whereas fluctuations are absent at 12 m and 15 m. This demonstrates progressive thermal equilibrium establishment as distance increases. Temperature fluctuations gradually attenuate until achieving full equilibrium beyond 12 m, where formation temperatures become decoupled from injection fluctuations.

Fig.6 depicts formation temperature profiles between wells at distinct temporal stages. Fig.6a displays the temperature distribution during daytime high-temperature injection, while Fig.6b corresponds to nighttime low-temperature injection. The injection well vicinity exhibits temperature responses synchronized with injection conditions: temperature elevation during high-temperature injection and decline during low-temperature injection. Crucially, temperature profiles beyond 10 m from the injection well become consistent between Fig.6a and 6b. This aligns with Fig.5 observations, confirming that temperature fluctuations induced by injection variations are confined to near-well regions (<10m). Through thermal attenuation within the formation, fluctuating temperatures progressively stabilize, demonstrating the aquifer storage system's capacity to convert variable energy inputs into stable thermal output.

Additionally, interwell temperatures evolve periodically over time, as demonstrated in Fig.7. The stratum nearest the injection well exhibits initial temperature elevation, followed by progressive thermal propagation toward the production well. Ultimately, the system approaches dynamic equilibrium. Cross-referencing Fig.6 reveals that formation temperatures near the injection well (but beyond the 10m equilibrium threshold) stabilize earliest, with the stabilized zone expanding temporally. Critically, equilibrium temperatures decrease proportionally with distance from the injection well. The temperature of the fluids produced from the production well is notably lower than the equilibrium temperature in its immediate vicinity, a phenomenon attributed to the fact that the temperature of the adjacent geological formation on the right remains unaffected.

The equilibrium temperature reaches its maximum near the injection well, experiencing minimal heat loss. This locus thus

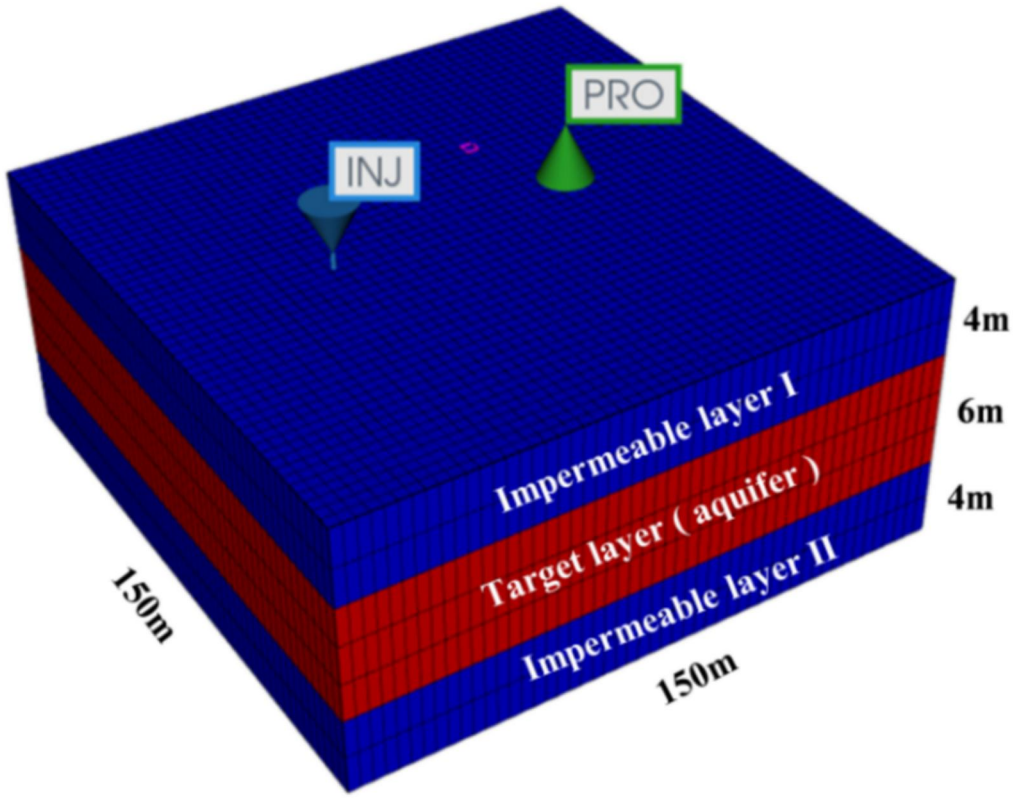

Fig. 4 Numerical model

Tab. 1 Parameters of base case

Parameter	Impermeable layer I	Target layer	Impermeable layer II
Permeability [mD]	1	100	1
Porosity	0.01	0.15	0.01
Volumetric heat capacity of rock [J/(m³·°C)]	2.35e6	2.35e6	2.35e6
Thermal conductivity of rock [J/(m·day·°C)]	1.5e5	1.5e5	1.5e5
Thermal conductivity of water [J/(m·day·°C)]	5.6e4	5.6e4	5.6e4
Initial temperature [°C]	70	70	70
Layer thickness [m]	4	6	4

provides a reference for correlating injection and equilibrium temperatures. Fig.5 further indicates an equilibrium temperature of 90°C, while the converted thermal energy of injected water averages 90°C. This equivalence indicates that equilibrium temperature is governed by the average thermal energy of injected water.

4.2 Temperature evolution of production well

When employing the ATES for energy balance, two factors must be considered: the production temperature and the response time of the system. The production temperature represents the system's ultimate available heat flow, which establishes its effectiveness. The economy of the system is determined by the response time, which is the length of time it can achieve effective heat flow after operation. Fig.8 shows the temperature curve of the production, including the change in the production temperature with time and the change in the heating rate (Eq.9) with time.

$$HR = \frac{T_{i+1} - T_i}{t_{i+1} - t_i} \tag{9}$$

where, HR is the heating-up rate, °C/day. T is the production temperature; T_{i+1} is the production temperature at time $i+1$; and T_i is the production temperature at time i, °C; t is the time, day.

As shown in Fig. 8, the production temperature curve exhibits a "stability-rise-stability" trend while the heating-up rate curve demonstrates a "stability-rise-decrease-stability" pattern. Therefore, the temperature curve can be divided into four stages based on the trend of changing temperature and the heating-up rate curve. Stage A (Low-Temperature Stabilization) occurs

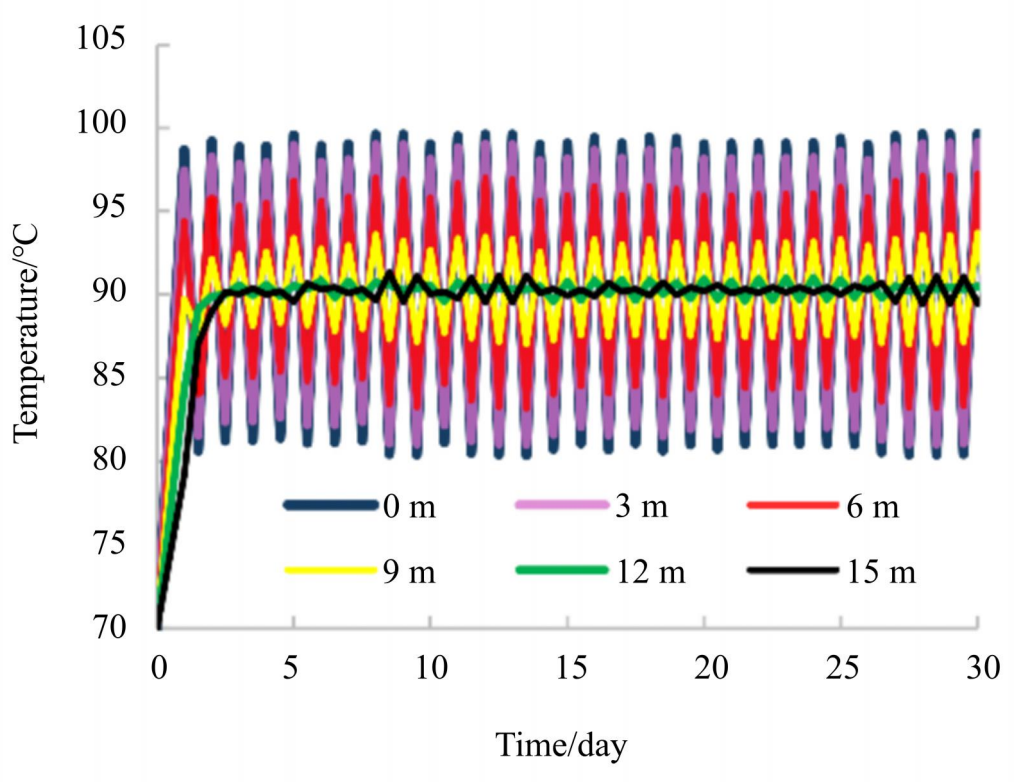

Fig. 5 Temperature variation around injection well

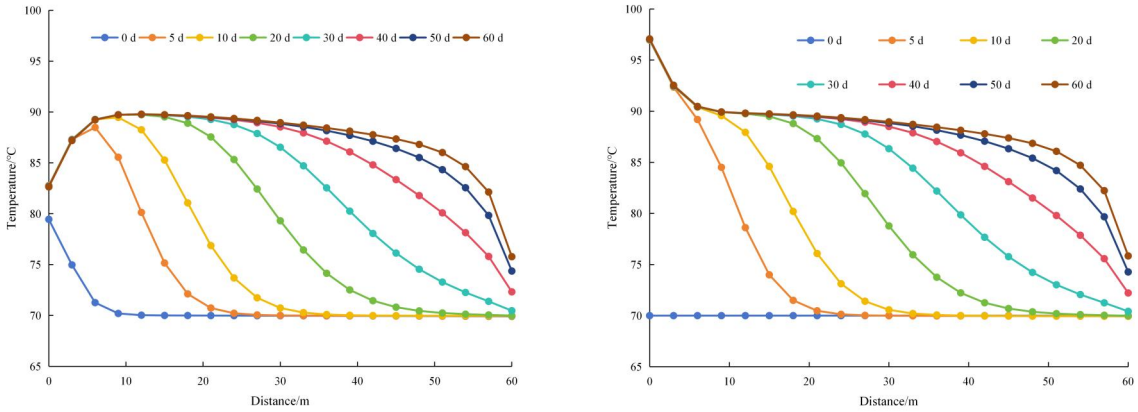

(a) Temperatures during the day (b) Temperature during the night

Fig. 6 The evolution of formation temperature between wells

before injected water breakthrough, with production well yielding native formation water at 70°C. During Stage B (Rapid Heating), the injected water reaches the production well during this stage. The initial temperature of this stage is lower because the heat of the injected water is exchanged with the formation rock along the flow channel. It results in the water's temperature being close to the temperature of formation when it reaches the production well. However, convective heat transfer occurs in the thermal reservoir of the aquifer. After the injection well and the production well are interconnected, the temperature difference between the subsequent water and the rock stratum gradually decreases. Stage C (Slow Heating) features converging rock-fluid temperatures along seepage paths that significantly reduce interfacial heat transfer, causing the heating rate to peak before declining as rising production well temperatures diminish thermal gradients. Stage D (High-Temperature Stabilization) begins when the formation temperature field approaches equilibrium. Currently, the production temperature exhibits minimal temporal variation, characteristically representing the final output temperature and simultaneously signifying achievement of steady-state conditions. Consequently, this research focuses on production temperatures after one year of operation and examines parametric influences thereon.

Response time analysis remains critical. As the heating-up

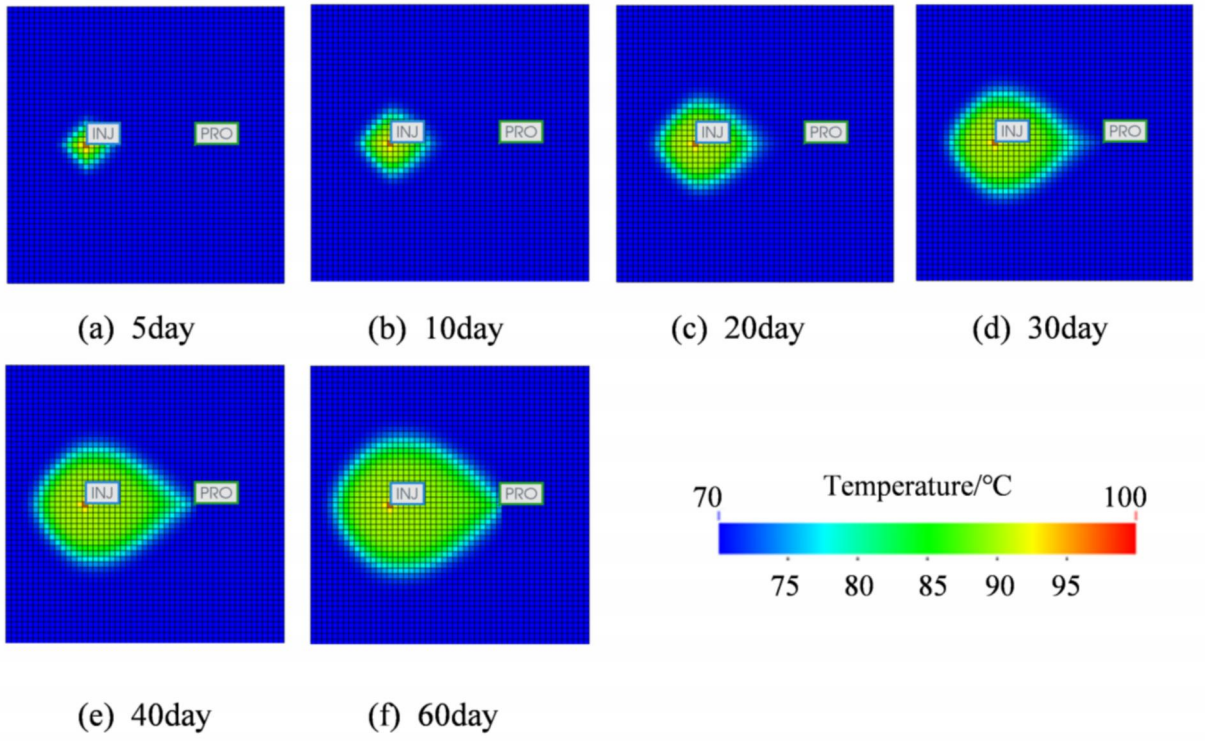

Fig. 7 The temporal and spatial evolution of temperature

rate curve indicates, production well heating rates decelerate after peaking, asymptotically approaching steady-state conditions. Consequently, this research investigates the timing of maximum heating rates and analyzes parametric influences on response time. Notably, while temperature profiles stabilize, minor heating rate fluctuations persist due to input energy variability. Nevertheless, such fluctuations exert negligible influence on time-dependent variations.

Therefore, the time corresponding to the maximum HR is defined as the response time t_R of the system. To determine the response time, the index k corresponding to the maximum HR is first identified as:

$$k = \underset{i=1}{\operatorname{argmax}} (HR_i) \tag{10}$$

Here, the $\arg\max(x)$ returns the index at which the variable x reaches its maximum value.

Substituting Eq. 9 into Eq. 10 yields:

$$k = \underset{i=1}{\operatorname{argmax}} \left(\frac{T_{i+1} - T_i}{t_{i+1} - t_i} \right) \tag{11}$$

Based on the above definition of response time,

$$t_R = t_k \tag{12}$$

Therefore, the system's response time is obtained by substituting Eq. 11 into Eq. 12:

$$t_R = t_{\underset{i=1}{\arg\max}((T_{i+1}-T)/(t_{i+1}-t_i))} \tag{13}$$

5 Parameter analysis of influence factors

5.1 Effect of injection temperature

The analysis above demonstrates how injection temperature impacts both the formation temperature distribution and production temperature. Five distinct schemes—each comprising low-temperature injection at 80 °C paired with high-temperature injection at either 100 °C, 110 °C, 120 °C, 130 °C, or 140 °C—were implemented to examine injection temperature impacts. The computational results for these schemes are presented in Fig. 9.

In the basic case, it is possible to stabilize the temperature in the formation 15 meters from the injection well. The temperature is correlated with the average energy of the injection. The time-varying temperature curve at 15m from the injection well is depicted in Fig 9a to further elucidate the reaction. The figure illustrates how temperature curve is smooth and fluctuation-free when the temperature difference is small (100 °C and 110 °C). With the increase of injection temperature fluctuation, the temperature curve shows significant fluctuation, and the greater the temperature difference, the greater the fluctuation. This implies that the distance of formation balance will be impacted by injection temperature fluctuations. The greater the temperature fluctuation, the longer the distance required for temperature equilibration. Furthermore, the five schemes yield an approximate equilibrium temperature of 90 °C, 95 °C, 100 °C, 105 °C, and 110 °C. Thus, the temperature of formation can be thought of as the injection of the average temperature in the formation equilibrium stage. It is the average value of the heat in the high-temperature injection stage and the low-temperature injection stage. The following can be used to express the rela-

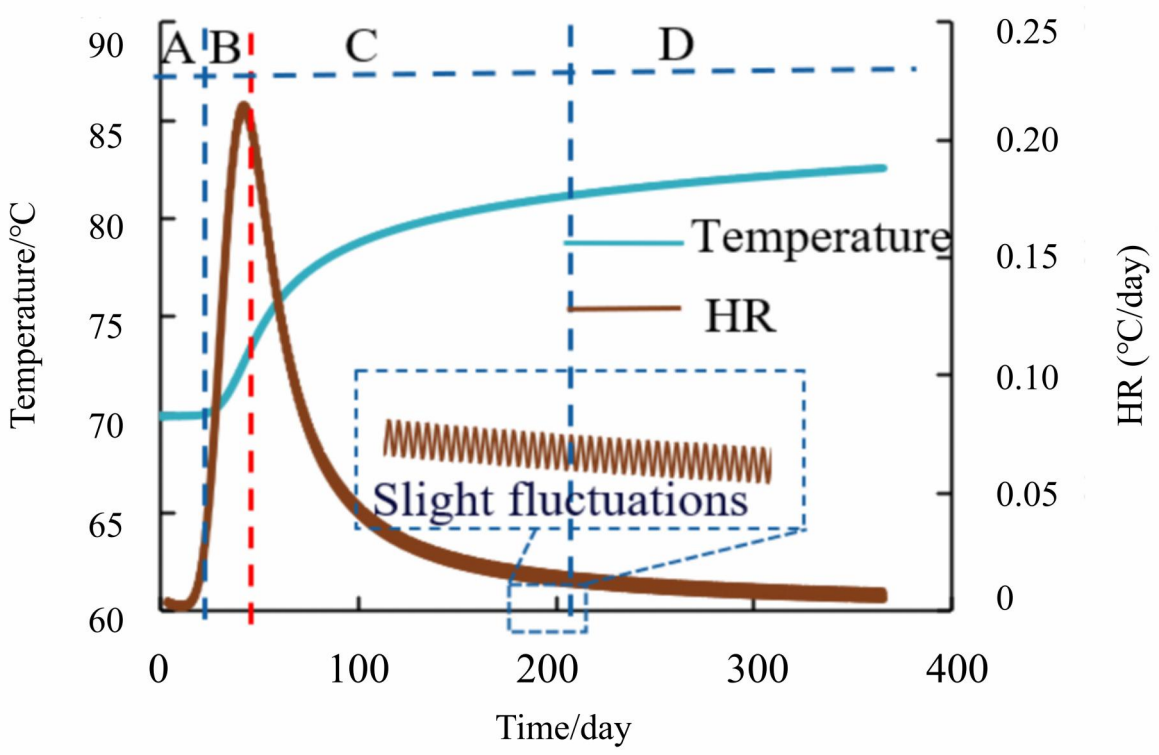

Fig. 8 Temperature curve of production

tionship between injection and formation temperatures.

In the base case, the formation temperature stabilizes at 15 meters from the injection well. This stabilized temperature correlates with the average thermal energy of the injected water. To further characterize this zone's response, Fig. 9a plots the temporal temperature evolution at 15 meters. The figure demonstrates smooth, fluctuation-free behavior under small injection temperature differences (100°C and 110°C). As the injection temperature fluctuation increases, the temperature curve at this location exhibits significant fluctuations. And the greater the temperature difference, the greater the volatility. This means that the fluctuation of injection temperature will affect the equilibrium distance. The greater the temperature fluctuation, the farther the distance required for temperature fluctuations to be balanced. Furthermore, the five schemes yield equilibrium temperatures of approximately 90°C, 95°C, 100°C, 105°C, and 110°C. Thus, the equilibrium temperature represents the time-averaged thermal value between high- and low-temperature injection stages, equivalent to the mean injection temperature during formation equilibrium. The relationship is quantified by the following equation:

$$T_a = \frac{\sum T_j t_j}{\sum t_j} \tag{14}$$

where, T_a is the average temperature of the formation, °C; T_j is the injection temperature in t_j time, °C; t_j is the duration of the j-th temperature stage, h.

Fig. 9b illustrates the temporal variation of production temperature. During Stage A (Low-Temperature Stabilization, Fig. 8), the production well yields native formation water at constant temperature. Subsequently, the temperature differential progressively widens between rapid heating (Stage B) and attenuated heating (Stage C) phases, stabilizing during Stage D (High-Temperature Equilibrium). Fig. 9c quantifies production temperature and heat loss (defined as the difference between production temperature and average injection temperature) after one year of operation, confirming a positive correlation between production temperature and daytime high-injection temperatures. Notably, production temperatures consistently remain below average injection temperatures, inducing conductive heat loss to the formation. As injection temperature increases, the proportional heat loss along the flow path rises synchronously. This occurs because when average injection temperatures exceed formation temperatures, energy transfers to surrounding formations at rates directly proportional to the temperature gradient—higher gradients accelerate conductive heat dissipation. Consequently, although high-temperature injection enhances thermal flux, it concomitantly amplifies heat loss magnitudes.

Fig. 9d depicts the heating rate evolution over time. The production well's heating rate increases with higher injection temperatures: at 100°C the maximum heating rate is 0.2°C/day, rising to 0.6°C/day at 140°C. The response time of system shows minimal sensitivity to injection temperature variation. This flow-dominant behavior is evidenced by consistent timing of peak heating rates across all temperature schemes. Furthermore, heating rate fluctuations exhibit temperature-dependent amplification patterns—both injection temperature variability and corresponding heating rate oscillations intensify progres-

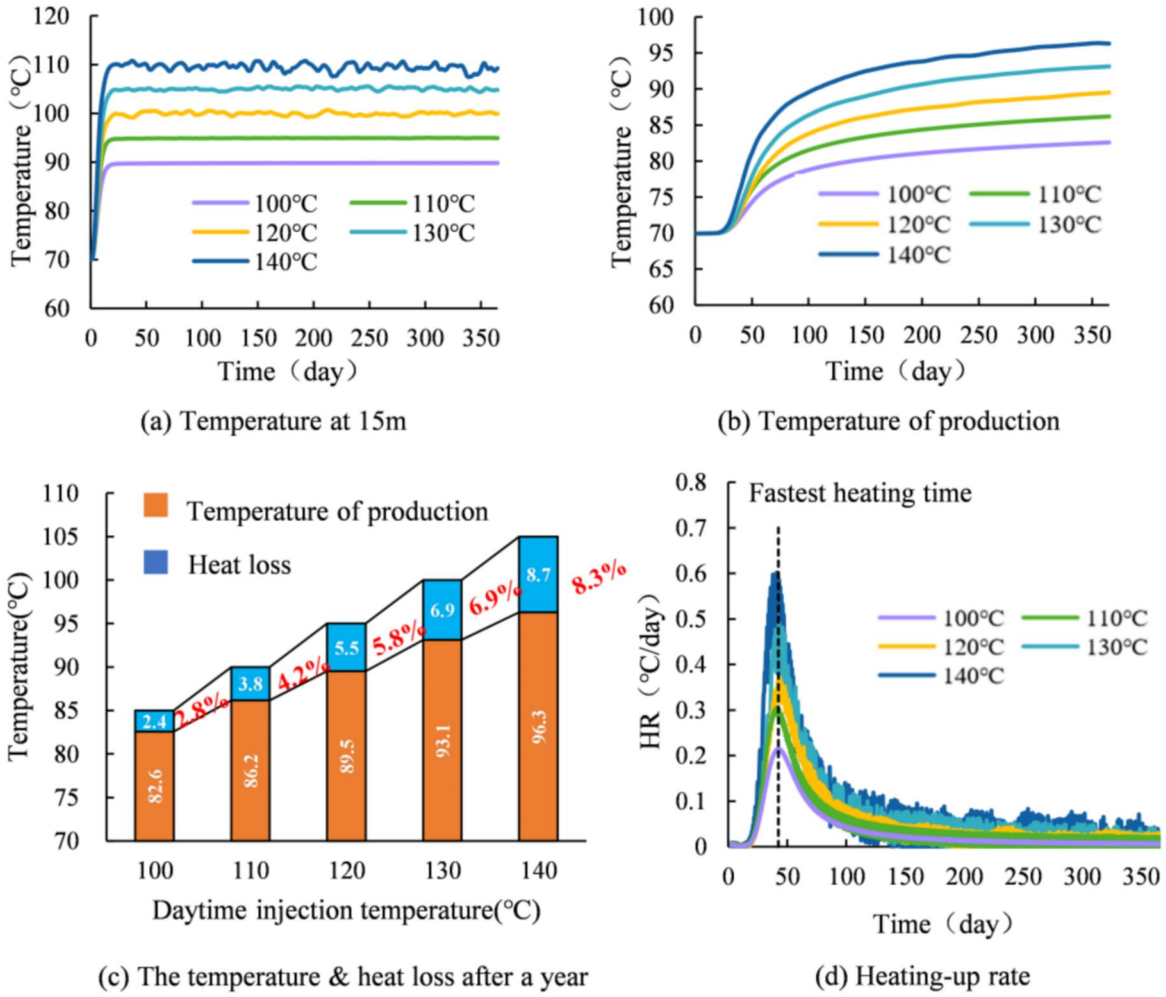

Fig. 9 Temperature at different injection temperatures

sively with increasing injection temperatures.

In conclusion, both the formation temperature field and production temperature are influenced by the injection temperature. Greater injection temperature fluctuations increase the equilibrium distance and amplify heating-up rate fluctuations. Additionally, the temperature of produced water is closely correlated with the thermal energy of injected fluid. Higher average injection temperatures elevate production temperatures but intensify heat loss. Moreover, temperature fluctuations have negligible impact on response time.

5.2 Effect of operation pressure

5.2.1 Effect of injection pressure

Injection pressure constitutes one modifiable production parameter. To analyze its influence on production temperature and response time, six injection pressure schemes were implemented: 14.5, 15.0, 15.5, 16.0, 16.5, and 17.0 MPa, with production pressure maintained at 11 MPa. Fig. 10 illustrates the temperature profiles at various injection pressures.

Fig. 10a presents the production temperature curve over time. During the low-temperature stable stage, production temperature remains constant as formation water dominates the flow. When injected water reaches the production well, production temperature begins to rise. With increasing injection pressure: (1) temperature rise initiates earlier, (2) curve slope steepens, and (3) ultimate temperature elevates. Consequently, injection pressure positively correlates with production temperature. Fig. 10b depicts the heating rate curve, showing that increased injection pressure elevates the peak heating rate and advances the timing of peak occurrence. Fig. 10c summarizes the maximum heating rates and corresponding peak times (defined as the time to reach maximum heating rate) for each injection pressure. The maximum heating rate exhibits a linear positive correlation with injection pressure, while peak time shows a negative correlation. These relationships are characterized by quadratic functions with $R^2 = 1$, confirming an exact fit.

Fig. 10d characterizes the inter-well formation temperature distribution after one month of injection to assess injection pressure effects on production temperature. The temperature field in the figure the is during the high-temperature injection stage. The temperature curves in the formation near the injection well basically coincide. But as the distance increases, the formation temperature is higher under high injection pressure condition-

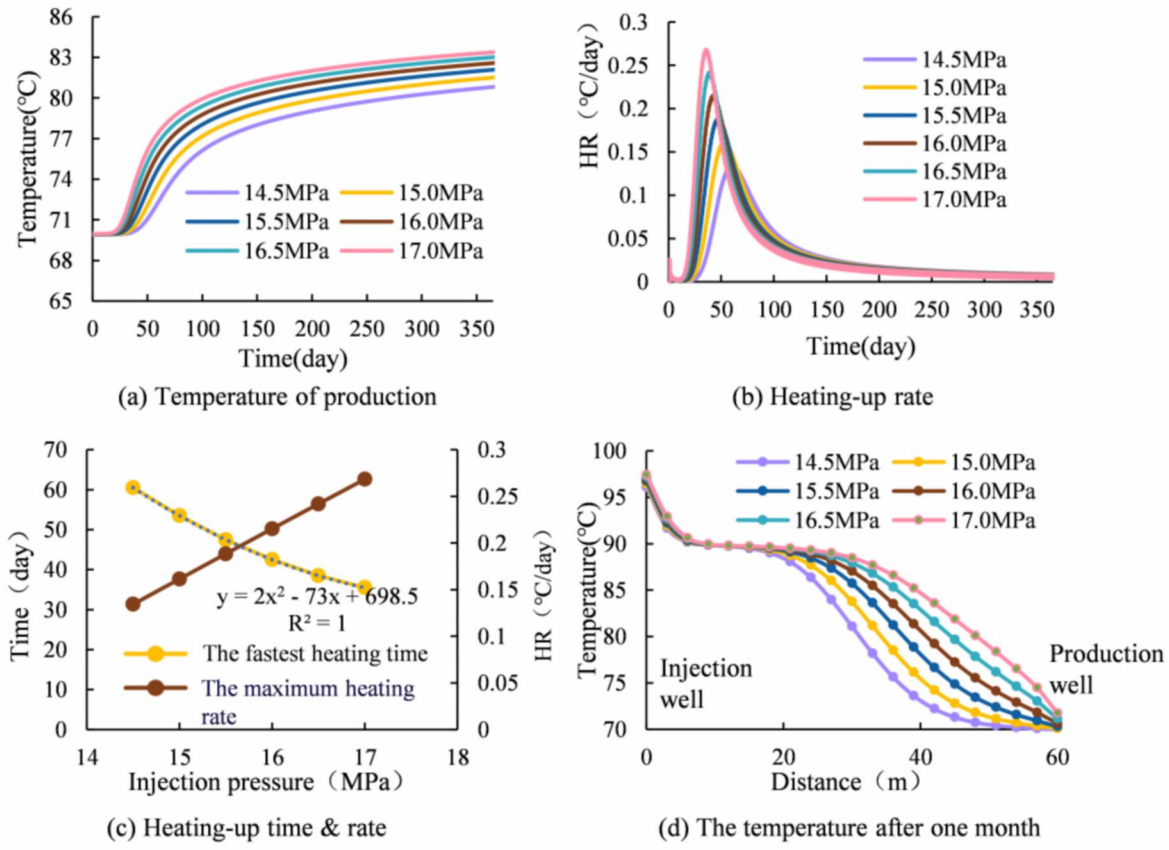

Fig. 10 Temperature under different injection pressures

s. This occurs because increased injection pressure amplifies the injection-production pressure differential, accelerating fluid flow rate. Given that aquifer thermal transfer is primarily governed by convective flow, expedited fluid movement enhances thermal propagation from injection to production wells, thereby expanding the heated formation volume and reducing response time.

In summary, injection pressure significantly influences production temperature and heating rate. Elevated injection pressure reduces response time, accelerates heating rates, and increases production temperatures. Quantitatively, the response time is negatively connected with injection pressure and meets the connection of quadratic curves, while the maximal heating-up rate has a linearly positive correlation with injection pressure.

5.2.2 Effect of production pressure

Production pressure constitutes another adjustable operational factor. Six production pressure schemes—10.0, 10.5, 11.0, 11.5, 12.0, and 12.5 MPa—were implemented to assess their impacts on production temperature and response time, with injection pressure maintained constant at 14 MPa. Temperature profiles under varying production pressures are illustrated in Fig. 11.

Fig. 11a depicts the production temperature curves under varying production pressures. During the low-temperature stable stage, production temperature remains unchanged. When injected water reaches the production well, temperature rise initiates earlier at lower production pressures. Ultimately, reduced production pressures yield higher terminal temperatures, establishing an inverse correlation between production pressure and terminal temperature. Fig. 11b presents the heating rate evolution, showing decreased peak heating rates and delayed peak times with increasing production pressure. Fig. 11c summarizes the relationship between production pressure versus maximum heating rates and peak timing. The data confirms: (1) a positive correlation between production pressure and time to peak heating rate, and (2) a negative correlation between production pressure and maximum heating rate. Collectively, lower production pressures accelerate heating rates and shorten response times.

Fig. 11d extracts the temperature distribution during high-temperature injection after one month. A distinct temperature fluctuation zone exists near the injection well, where injection temperature governs thermal behavior within this range. Formation temperature achieves equilibrium with increasing distance from the injection well, stabilizing locally at 90°C. Distant formation temperatures depend on thermal transfer processes as full equilibrium remains unattained. Reduced production pressure increases the injection-production pressure differential, accelerating formation fluid flow which intensifies convective heat transfer. Consequently, thermal propagation accelerates, response time shortens, and the high-temperature formation

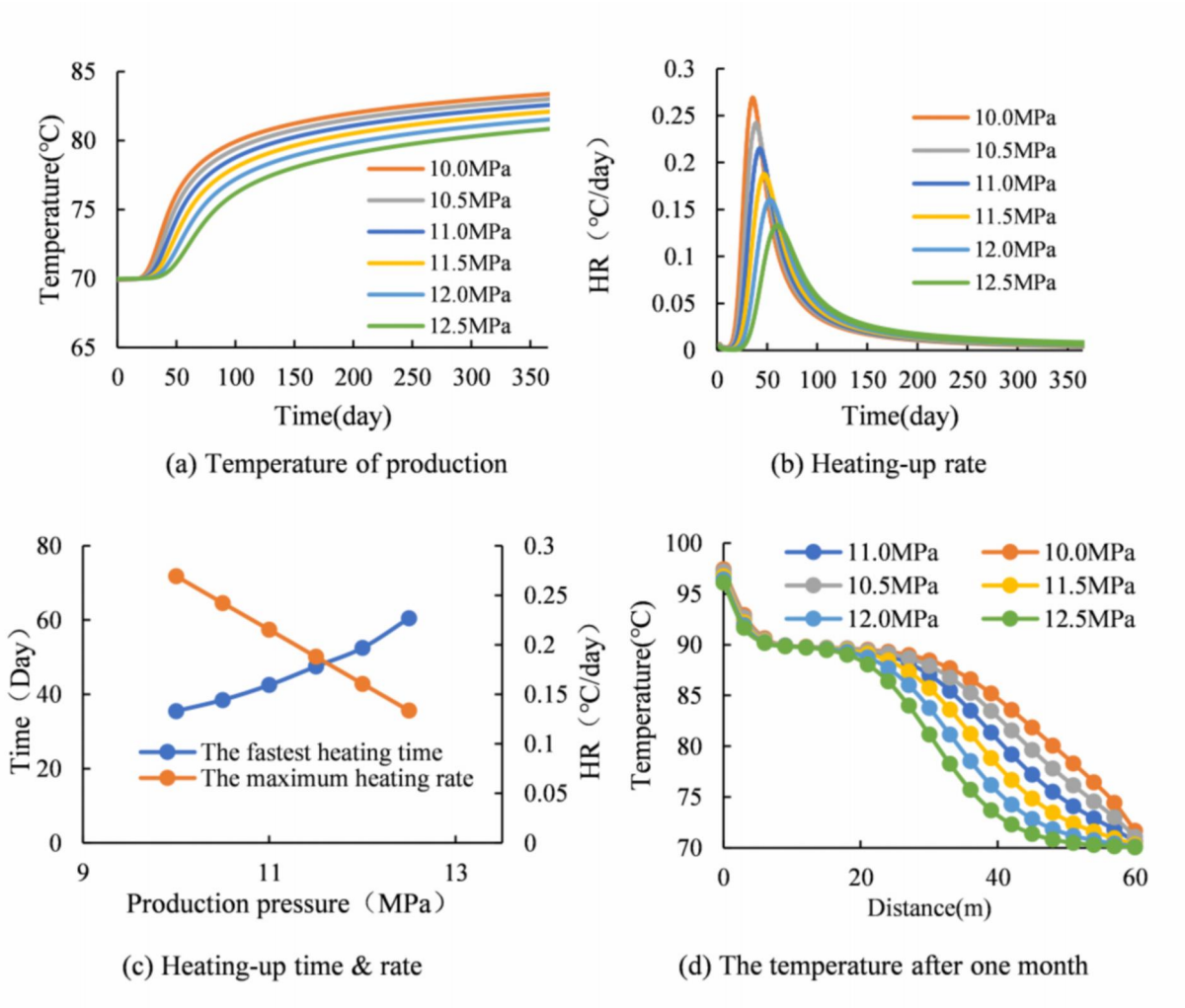

Fig. 11 Temperature under different production pressures

zone expands.

In conclusion, production pressure significantly governs both the temperature and heating rate of the production well. Elevated production pressure extends response time, decelerates heating rates, and reduces production temperatures.

5.2.3 Effect of pressure difference

The flow of high-temperature water through aquifers is a process of convective heat transfer between the fluid and rock matrix. Adjustments to either injection or production pressure fundamentally alter the injection-production pressure differential. Therefore, simulation results from these two pressure adjustment scenarios are consolidated into a unified analysis of pressure differential impacts. Production temperatures and heating rates across varying pressure differentials are compiled in Fig. 12.

Fig. 12a presents production temperatures after one-year operation under varying injection-production pressure differentials. Production temperature increases with larger pressure differentials. Crucially, identical differentials yield matching production temperatures regardless of whether injection or production pressures are modified. Fig. 12b characterizes heating rate behavior: greater differentials elevate maximum heating rates and advance peak timing, confirming accelerated thermal response and shortened reaction times. Data consistency under equal differentials—whether adjusted via injection or production pressure—demonstrates that pressure differential universally governs thermal performance. It should be noted that these conclusions assume negligible hydro-mechanical coupling and fixed groundwater flow direction. While practical applications must account for these factors, the identified pressure differential-temperature relationships retain significant engineering guidance value.

Darcy's Law governs how injection-production pressure differentials influence inter-well flow characteristics. Fig. 13a presents daily production rates under varying pressure differentials, demonstrating proportional increases in production rates with larger differentials. Crucially, identical differentials yield equivalent daily production rates regardless of injection/production pressure adjustments. Consequently, elevated pressure differentials simultaneously enhance both daily production volumes and production temperatures.

However, the production temperature is lower than the average injection temperature, and the heat is lost during the formation equilibrium conversion process. The heat loss rate

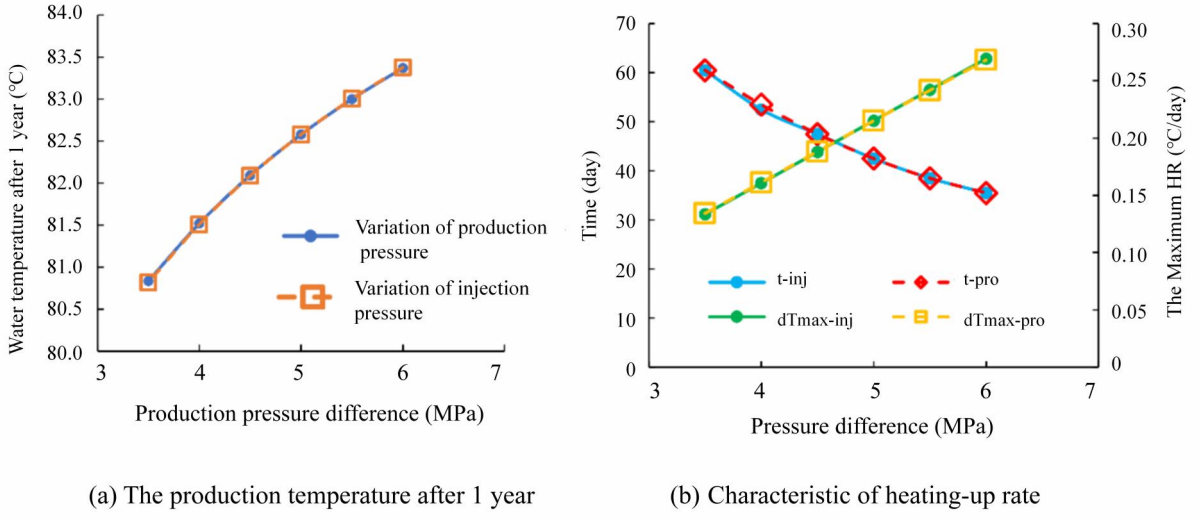

(a) The production temperature after 1 year (b) Characteristic of heating-up rate

Fig. 12 Temperature under different injection-production pressure differences

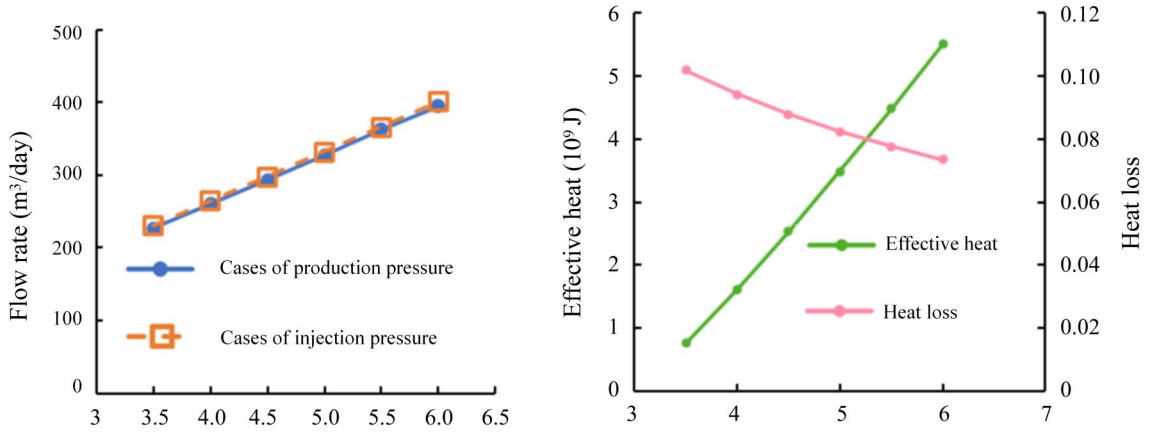

(a) The daily production (b) Effective heat & heat loss

Fig. 13 Flow and heat under different injection-production pressure differences

is defined as follows:

$$I = \frac{Q_{in} - Q_{out}}{Q_{in}} \tag{15}$$

where, Q_{in} is the heat of injection, J; Q_{out} is the heat of the production, J; L is the heat loss rate, dimensionless. Q_{in} and Q_{out} are expressed as follows.

$$Q_{in} = cm_{in1}T_{in1} + cm_{in2}T_{in2} = cm_{in}T_a \tag{16}$$

$$Q_{out} = cm_{out}T_{out} \tag{17}$$

In the simulation, an injection-production balance is set with a ratio of 1:1. It is also assumed that the injection time for high-temperature is the same as that for low-temperature, thus satisfying the following equation:

$$m_1 = m_2 = 0.5m_{out} \tag{18}$$

$$m_{out} = \rho V \tag{19}$$

where, c is the volumetric heat capacity, J/(kg·° C); m_1 is the quality of injection in the high-temperature injection stage (12h), kg; m_2 is the mass of injected water in the low-temperature stage (12h), kg; m_{out} is the quality of production within 24 hours, kg; ρ is the density of water, 971 kg/m^3 is taken; V is the volume of daily production, which is equal to the daily production, m^3.

Varying injection-production pressure differentials yield distinct daily production rates. Higher production volumes and temperatures correspond to greater thermal energy extraction. Given that organic Rankine cycle systems can utilize low-grade heat resources as low as 80°C for power generation, this threshold defines economically recoverable heat. The effective

thermal energy is thus defined as:

$$Q_E = cm_{out}(T_{out} - T_E) \quad (20)$$

where T_E is the effective temperature, °C, set at 80 °C in this study. T_{out} is the production temperature, °C; Q_E is the effective heat, J.

Using the preceding equation, daily heat loss rates and effective thermal energy can be calculated. Fig. 13b plots these parameters under varying injection-production pressure differentials. Results demonstrate reduced heat loss rates and enhanced effective thermal energy with increasing pressure differentials. Complementary Fig. 13a shows that elevated differentials accelerate formation seepage velocity. This flow acceleration shortens fluid transit time between wells, reducing heat dissipation during convective heat transfer between water and rock matrix. Furthermore, greater pressure differentials increase injected water volumes, enabling rapid thermal replenishment that diminishes rock-fluid temperature differences during subsequent flows. Consequently, high pressure differentials minimize system heat loss while maximizing effective thermal energy. Therefore, optimizing pressure differentials within geomechanical stability and economic constraints significantly enhances thermal recovery efficiency through three mechanisms: increased effective energy yield, reduced thermal dissipation, and shortened response time.

5.3 Effect of permeability

Permeability represents an intrinsic formation property governing fluid behavior. To investigate its impacts on production temperature and heating rate, six permeability schemes were modeled: 60, 80, 100, 120, 140, and 160 mD. Fig. 14 characterizes thermal properties under these permeability conditions.

Fig. 14a illustrates production temperature curves across varying permeabilities. Low permeability regimes delay temperature initiation, manifesting in reduced curve slopes and lower terminal temperatures. Temperature elevation directly correlates with permeability enhancement. However, incremental permeability increases (per +20 mD) yield greater thermal gains in low-permeability formations than in high-permeability systems. Consequently, permeability enhancement efficiently elevates temperatures in low-permeability zones, whereas equivalent adjustments in high-permeability reservoirs exhibit diminishing thermal returns. This demonstrates the critical need to avoid low-permeability domains during site selection.

Fig. 14b presents heating rate curves, revealing that low-permeability formations exhibit reduced peak heating rates and delayed peak timing. Increased permeability elevates maximum heating rates, advances peak occurrence time, and shifts curve apexes leftward. These relationships are quantified in Fig. 14c, confirming that higher permeability increases maximum heating rates while decreasing peak timing (fastest heating time). Fig. 14d illustrates inter-well temperature fields after one-month injection, demonstrating permeability's control over thermal propagation: greater permeability enhances heat transfer efficiency from injection to production wells. Notably, at 60 mD permeability, measured temperature reaches only 79.96°C—below the 80°C operational threshold. Consequently, low-permeability systems yield inadequate temperatures for practical applications. Therefore, high-permeability reservoirs achieve shorter response times and higher production temperatures, establishing their priority in site selection.

Integrated pressure analysis confirms that inter-well flow rate critically governs production temperature. Fig. 15a quantifies daily production across permeability variations: production increases proportionally with permeability enhancement. For the 160 mD scenario, production is capped at 500 m^3/day to ensure equipment integrity. Other permeability conditions maintain linear flow-permeability relationships. Given the fixed 1:1 injection-production ratio, production rates directly characterize formation flow behavior. Higher flow rates increase thermal energy injection while accelerating fluid rate, thereby accelerating formation temperature escalation. Consequently, permeability fundamentally modulates formation transport properties: high-permeability reservoirs exhibit elevated flow rates, expedited thermal propagation, enhanced heating rates, and reduced response times.

Production volume and temperature collectively determine system thermal output efficiency. Fig. 15b analyzes permeability impacts on effective thermal energy and heat loss rates. At 60 mD permeability, production temperatures fall below the 80°C threshold, resulting in zero effective thermal energy. Other permeability scenarios (> 80°C) yield calculable effective energy. Analysis confirms that higher permeability increases effective thermal energy while reducing heat loss rates—specifically decreasing from 12% at 60 mD to 6% at 160 mD. Notably, low-permeability regimes exhibit elevated heat loss rates, where permeability enhancement significantly reduces losses. However, the reduction in heat loss rate diminishes progressively with increasing permeability.

In conclusion, permeability governs formation seepage characteristics, consequently regulating formation flow rates. Convective heat transfer rates depend directly on these flow rates, thereby influencing production temperature, heating rate, heat output, and heat loss magnitude. Elevated permeability enhances production temperature while simultaneously reducing response time, accelerating heating rates, increasing effective heat recovery, and diminishing heat loss rates. Consequently, site selection should prioritize formations with maximal permeability.

5.4 Effect of porosity

Porosity is another inherent property of the formation. To examine the impact of porosity on the production temperature, six different porosity schemes 0.05, 0.10, 0.15, 0.20, 0.25, and 0.30 were established. Fig. 16 displays the results of production temperature and heating-up rate under various schemes.

Fig. 16a presents the production temperature curve evolving through four phases. Unlike pressure and permeability patterns, porosity conditions yield distinct thermal behaviors. During rapid heating, low-porosity formations initiate heating earlier with steeper temperature rise and higher initial temperatures. However, thermal crossover occurs in slow heating phase. The low-porosity systems exhibit reduced heating rates and

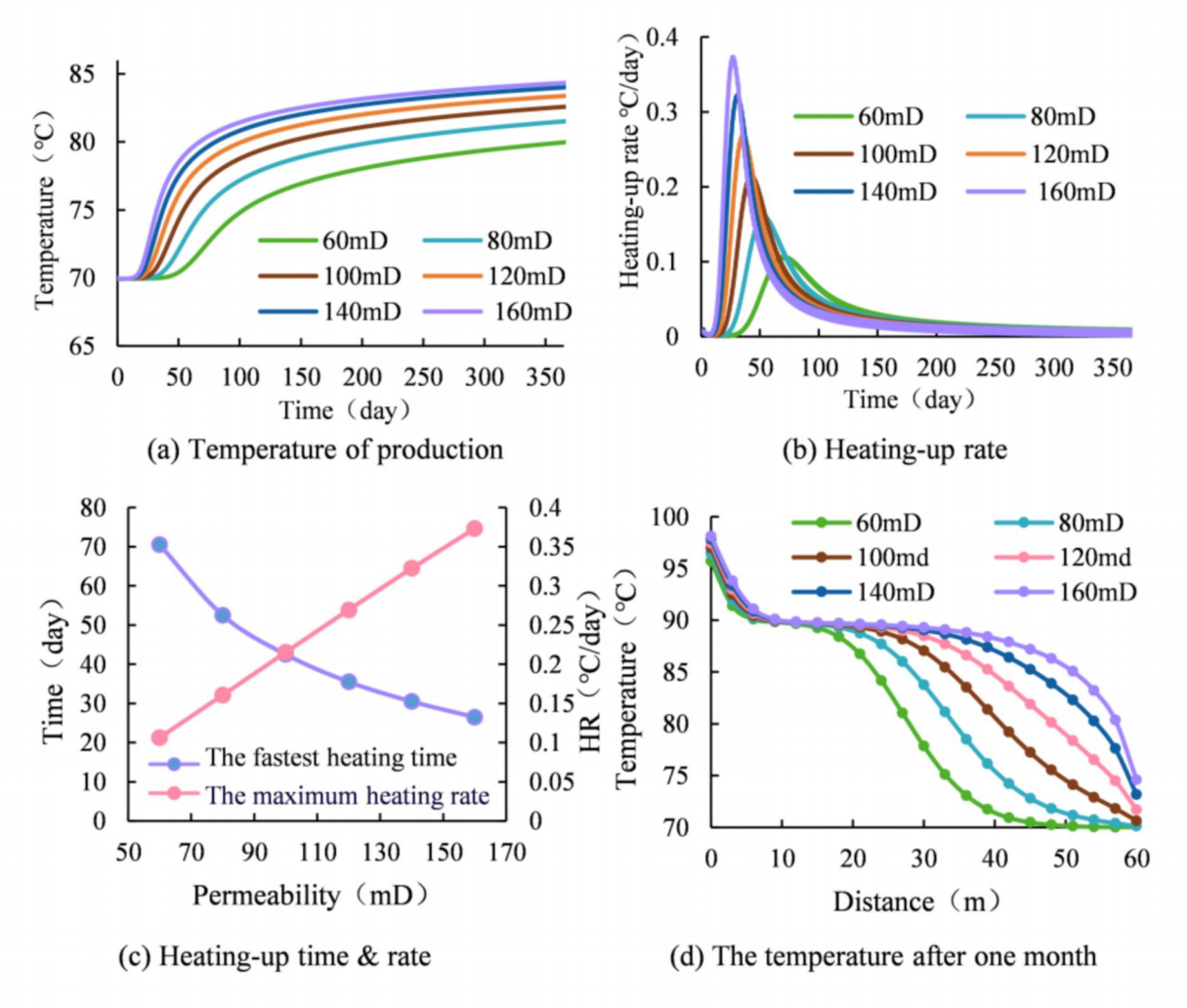

Fig. 14 Temperature under different permeability

marginally lower temperatures compared with high-porosity formations. After entering the high-temperature stable stage, the temperature difference under various operating conditions remains stable. The final production temperature under low porosity conditions is slightly lower than that under high porosity conditions. However, it is worth noting that porosity has little effect on the production temperature. And the temperature under different operating conditions is between 82-83 degrees. However, to reveal the influence of porosity, it is necessary to clarify the temperature response of produced water under different porosities. In summary, the influence of porosity on production temperature can be divided into two stages. In the rapid heating stage, the temperature of low porosity formations is higher than that of high porosity formations. As the temperature inside the formation reaches a thermal breakthrough, the temperature between the injection and production wells is interconnected, and the heating rate gradually decreases, entering a slow heating stage. Currently, the temperature increase of low porosity formations is smaller than that of high porosity formations, so the temperature of high porosity formations gradually increases. After entering the high-temperature equilibrium stage, the temperature continues to maintain the high porosity characteristics of the formation.

Fig. 16b depicts heating rate curves, revealing consistent peak heating rates across porosity variations with minimal peak timing differences. Unlike pressure and permeability scenarios exhibiting multi-decade peak time variations, porosity-induced differences remain under 10 days (e.g., 39.5 days at 0.05 porosity vs. 46.5 days at 0.30 porosity). This confirms porosity's limited influence on thermal dynamics. To elucidate underlying mechanisms, magnified views of rapid and slow heating stages are analyzed. During rapid heating, the 0.30 porosity curve exhibits the lowest position, indicating minimal heating rate. Conversely, in slow heating, the 0.05 porosity curve occupies the lowest position. This alignment with temperature curve responses stems from stage-specific heating rate differentials, which drive phased temperature variations. Porosity's thermal impact mechanisms are detailed in Section 6.

5.5 Effect of volumetric heat capacity

The volumetric heat capacity (VHC) of rock is an inherent property of formation. To analyze the influence of rock volumetric heat capacity on the production temperature, five

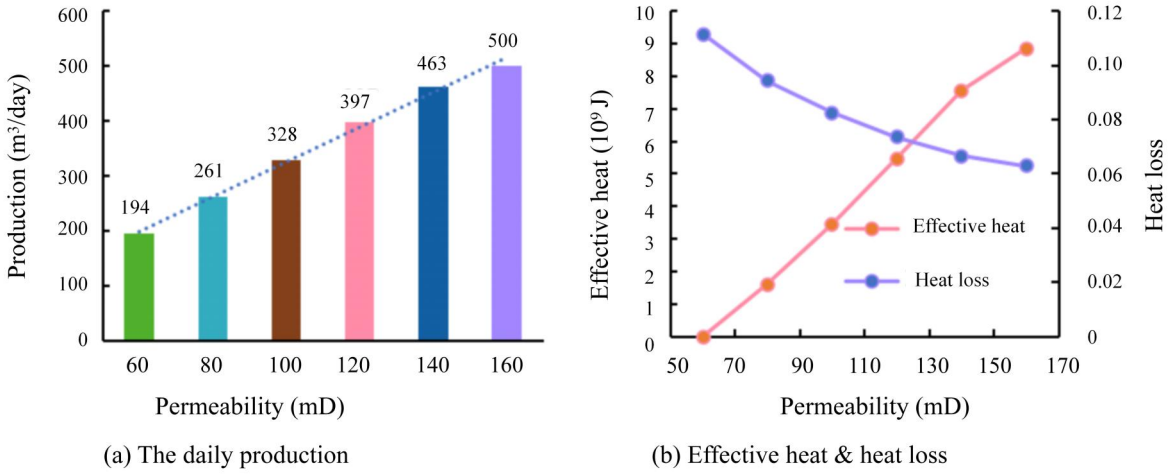

(a) The daily production (b) Effective heat & heat loss

Fig. 15 Characteristics of production and heat under different permeability

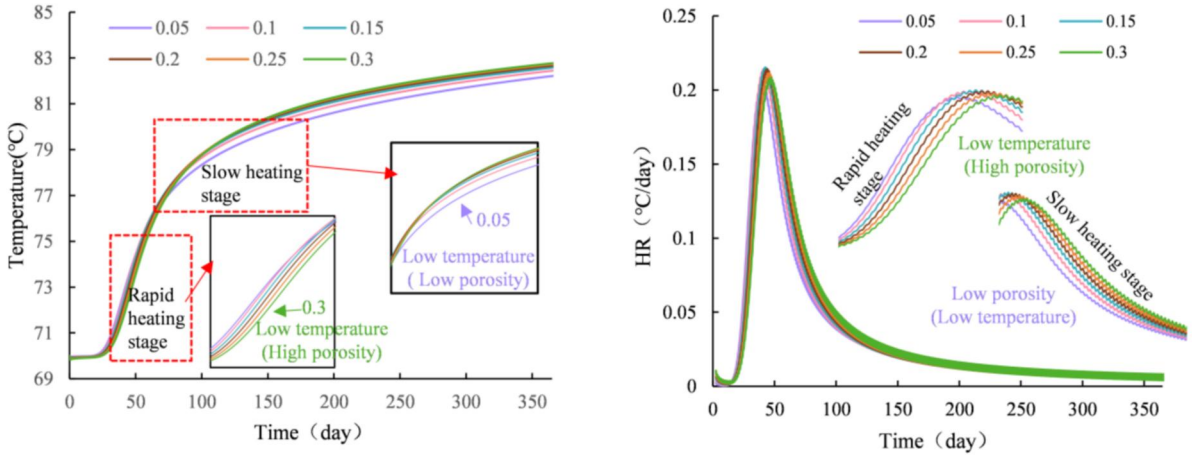

Fig. 16 Temperature under different porosity

schemes of VHC of 1.0e6, 1.5e6, 2.0e6, 2.5e6 and 3.0e6 J/(m^3·°C) were set up. The calculation results of the temperature and heating-up rate of different schemes are shown in Fig 17.

The production temperature curve is shown in Fig 17a. The temperature curve rising quicker in the rapid heating stage corresponds to the low VHC. Nevertheless, at the slow heating stage, the temperature curve corresponding to the low VHC is lower. This thermal response parallels porosity influences, with low-VHC temperature curves demonstrating distinct "initially fast, gradually slowing down" characteristics in production temperature curves. Then, the difference between the curves at the same time is stable during the high-temperature stable stage. So, the greater the VHC, the higher temperature after a year. In conclusion, the changes in production temperature are mainly manifested in the two stages of rapid heating and slow heating.

The heating rate under different cases is analyzed in Fig. 17b. As can be observed, in the rapid heating stage, the heating rate of formations with low VHC is fast, so the production temperature rises first. The low-VHC formation heats up more slowly than the formation with a high VHC after reaching the slow heating stage. The temperature ultimately surpasses this point because the temperature increase under high VHC conditions is greater than that under low VHC conditions. It should be noted that the VHC has minimal impact on the production temperature and heating-up rate when compared to the effects of seepage characteristics. The analysis here attempts to shed light on how temperature features are affected by VHC and conduct a thorough analysis.

In conclusion, VHC and porosity have comparable effects on the temperature. The percentage of voids in the skeleton of the rock is called porosity. The larger the porosity, the larger the voids within the rock skeleton, which means it can accommodate a larger volume of water. The VHC is the amount of heat required to be absorbed or released by a 1K temperature change per unit volume of rock. And it represents the capability of rock to hold heat. The amount of heat that the rock skeleton can absorb increases with the VHC. Both have the same property: the higher the porosity or VHC, the more heat can be stored per unit volume. As a result of their comparable effects on the

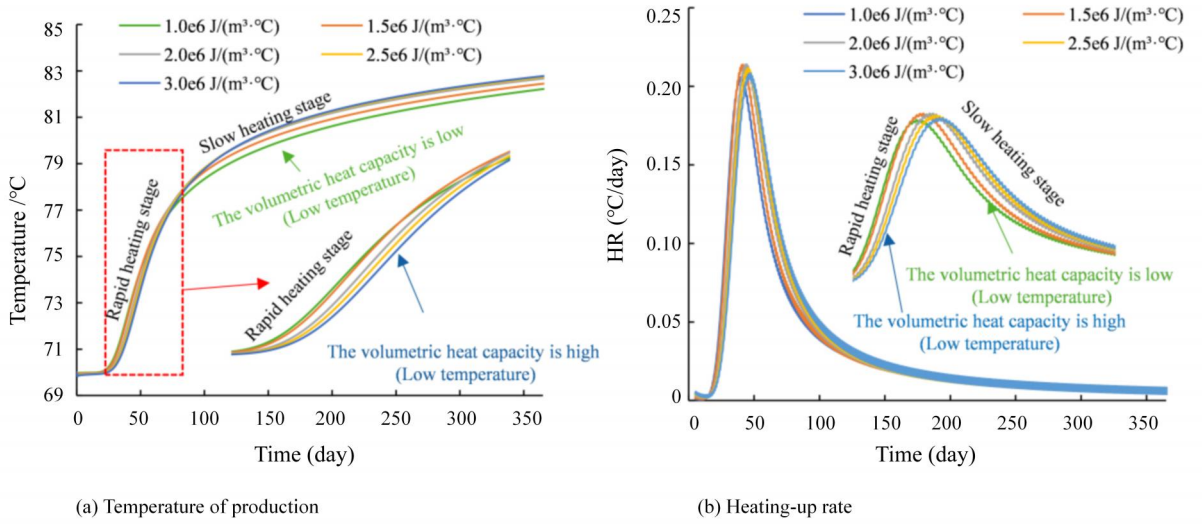

(a) Temperature of production

(b) Heating-up rate

Fig. 17 Temperature under different volumetric heat capacity

temperature as well as their shared features of porosity and VHC, these two factors can be considered as indicators of the heat storage capacity of the reservoir. The greater the thermal storage capacity of rocks, the more heat the rock layers will absorb from water. This slows down the transmission of formation temperature. The specific impact of VHC on temperature changes will be discussed in Section 6.

5.6 Effect of rock thermal conductivity

Thermal conductivity, a key parameter governing formation heat transfer efficiency, quantifies rock heat conduction capacity. To analyze its impacts, six thermal conductivity schemes were implemented: 100, 150, 200, 250, 300, and 350 kJ/(m·day·°C). Fig. 18 depicts thermal response profiles under these conductivity variations.

Fig. 18a presents the production temperature curve. Upon entering the rapid heating stage, temperatures escalate rapidly. Critically, low-thermal-conductivity scenarios exhibit the steepest temperature rise, while increasing conductivity reduces production temperatures. During the slow heating stage, low-conductivity systems maintain greater temperature gains than high-conductivity counterparts. These differentials stabilize upon reaching high-temperature equilibrium, with terminal temperatures inversely proportional to thermal conductivity. Complementary Fig. 18b quantifies production temperatures after one year, confirming an inverse correlation between conductivity and temperature. Notably, conductivity variations induce significantly larger temperature fluctuations in low-conductivity regimes than in high-conductivity formations.

Fig. 18c depicts heating rate evolution curves. Lower thermal conductivity yields higher heating rates, with the area under the heating rate curve quantifying production temperature. Reduced conductivity amplifies peak heating rates and expands curve-enclosed areas (Fig. 18c). Fig. 18d confirms thermal conductivity's negligible impact on peak timing (response time) but significant influence on heating magnitude. Consequently, conductivity modulates heating rates without altering response times.

Mechanistically, forced convection governs inter-well thermal transfer, dominating the production temperature response (detailed in Section 6). Thermal conductivity primarily regulates conductive heat losses within rock formations. Given rock conduction rates are orders of magnitude lower than water convection rates, rock conductivity minimally affects response times. However, higher rock conductivity intensifies thermal dissipation during fluid flow, reducing peak heating rates proportionally to energy loss.

6 Result and analysis

6.1 Summary of the influence of different factors

The injection temperature, pressure difference, permeability, porosity, volumetric heat capacity, and thermal conductivity are analyzed. The effects of various factors on the production temperature and response time are different. Their impact can be summarized in Tab. 2.

6.2 Analysis of the influence mechanism of various factors on production temperature

From a mechanistic perspective, production temperature dynamics are intrinsically governed by subsurface flow and heat transfer processes. As formalized by the energy conservation equation for saturated aquifers (Eq. 5), thermal losses during injection resolve into three distinct mechanisms: 1) Thermal absorption (Term I): Formation heat uptake driven by fluid-rock temperature differentials, quantified by apparent heat capacity (Eq. 6) with porosity and volumetric heat capacity (VHC) dependencies. 2) Convective heat transfer (Term II): Fluid-transported energy manifesting as production temperature, exclusively determined by flow velocity with governing parameters including injection-production pressure differential and permeability—exhibiting dominant influence on production temperature. 3) Thermal diffusion (Term III): Conductive dissipation modulated by apparent thermal conductivity (Eq. 7) through porosity/conductivity coupling. In summary, factor

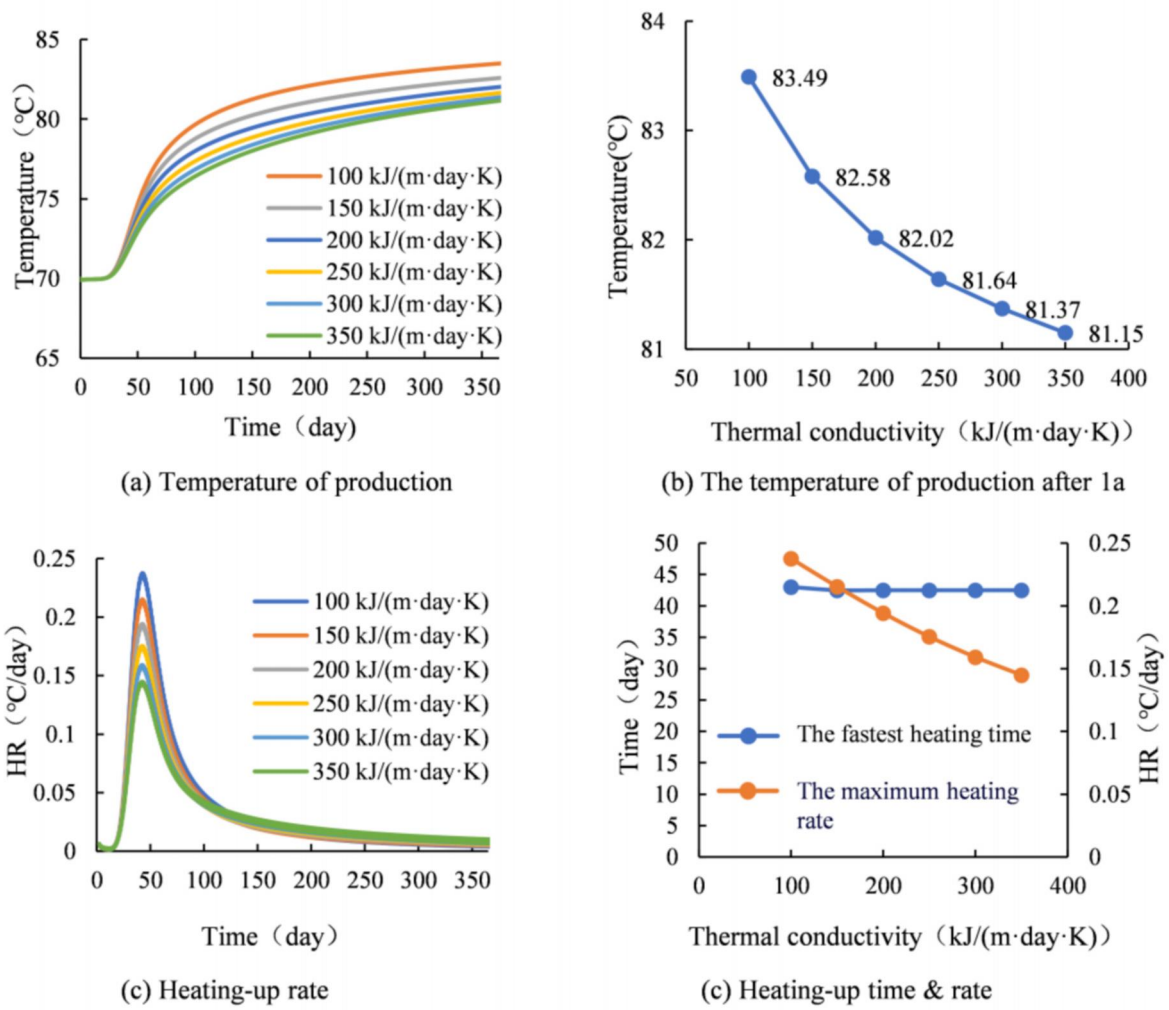

Fig. 18 Temperature under different thermal conductivity

Tab. 2 Analysis of the influence of different factors

Factors	Effect on production temperature	Effect on the heating rate
Injection temperature	Increases with injection temp.	Max heating rate ↑, Resp. time unchanged with inj. temp. ↑
Pressure difference (ΔP)	Increases with pressure difference	Max heating rate ↑, Resp. time advanced with ΔP ↑
Permeability	Increases with permeability	Max heating rate ↑, Resp. time ↓ with permeability ↑
Porosity	Initial Stage: High temp. with low porosity; Stable Stage: High temp. with high porosity.	Max heating rate constant, Resp. time slightly delayed with porosity ↑
Volumetric heat capacity (VHC)	Initial Stage: High temp. with low VHC; Stable Stage: High temp. with high VHC.	Max heating rate constant, Resp. time slightly delayed with VHC ↑
Thermal conductivity	Decreases with thermal conductivity	Max heating rate ↓, Resp. time unchanged with thermal conductivity ↑

significance ranking for production temperature: Injection temperature > seepage factors (pressure difference, permeability) > formation thermal conductivity > thermal storage factors (porosity, VHC). Response time is primarily controlled by fluid velocity, with minimal influence from thermal storage factors and negligible impact from injection temperature or thermal conductivity.

As specified in Table 2, injection temperature corresponds to the source/sink term in the governing equation. Elevated injection temperatures increase energy input to the formation,

thereby raising production temperatures. However, injection temperature variations negligibly impact thermal response time. Injection-production pressure differential and permeability exhibit consistent thermal influence mechanisms: both modulate temperature via fluid velocity control. Increased flow velocity reduces fluid retention time per unit volume within the formation, consequently diminishing thermal diffusion losses and elevating both production temperature and peak heating rates. Simultaneously, accelerated flow advances thermal breakthrough timing at production wells. Thus, convective fluid velocity decisively governs production temperature characteristics.

Complementing this understanding, porosity impacts temperature through dual-phase characteristics: low-porosity formations demonstrate higher initial temperatures, while high-porosity formations achieve superior equilibrium temperatures. During the initial thermal stage, fluid velocity dominates temperature dynamics. Reduced pore volume in low-porosity formations accelerates native water displacement, enabling earlier injected water breakthrough at production wells. Consequently, these formations achieve faster initial heating rates (implying marginally delayed thermal breakthrough with increasing porosity). In advanced thermal stages, thermal diffusion becomes predominant. Here, porosity governs both apparent heat capacity (Eq. 6) and apparent thermal conductivity (Eq. 7). Since rock's specific heat capacity and thermal conductivity exceed water's, low porosity elevates both parameters. Higher apparent heat capacity dampens temperature rise per unit energy input, while enhanced thermal conductivity intensifies thermal dissipation. Thus, low-porosity formations exhibit depressed temperatures during later stages. Parallel phenomena emerge in volumetric heat capacity (VHC) impacts, which exhibit similar dual-phase behavior: formations with low VHC achieve higher temperatures during initial thermal development, while high-VHC formations demonstrate superior thermal stability at equilibrium. According to equation 6, the VHC determines the apparent heat capacity. In the early stage, due to the temperature difference between the injected water and the formation, the formation needs to absorb the heat of the injected fluid to achieve temperature balance. The temperature at which the injected fluid reaches the production well is a reflection of the heat absorbed by the formation during the equilibrium process. Therefore, if the VHC is low, the apparent heat capacity is low, and the amount of heat absorbed to reach equilibrium with the fluid temperature is lower. As a result, the heat reaching the production well is greater, and the production temperature is higher. In the later stage, the temperature in the convective zone has reached equilibrium, and the heat loss of the injected fluid is mainly due to the heat diffusion to the periphery. At this point, under the same temperature conditions, a larger VHC stores more energy, and the temperature drop caused by transferring the same amount of heat outward is smaller. The smaller the temperature drop, the smaller the temperature gradient with adjacent strata. Therefore, in the later stage, the temperature gradient of high VHC formations is smaller and there is less thermal diffusion, allowing the formation to effectively maintain higher temperatures. So, in the later stage, the production temperature of high VHC formations will be higher.

The formation's heat conduction is influenced by thermal conductivity, and this has a big impact on the production temperature. The final temperature decreases with increasing thermal conductivity because it increases thermal diffusion to the periphery.

6.3 The dual-zone configuration

Building upon the analysis of production temperature influence mechanisms, injected hot water primarily transfers thermal energy to production wells via convective heat transfer. Thermal losses encompass formation heat absorption during thermal equilibration and conductive dissipation to peripheral regions, with residual heat reaching production wells through convective transport. During initial production stages, substantial thermal energy is absorbed by the formation to achieve equilibrium.

Upon reaching fundamental thermal equilibrium, primary heat dissipation shifts toward peripheral zones. As Fig.7 corroborates, post-equilibration in the well region establishes a distinct thermal zone exhibiting significant temperature differentials relative to surrounding formations. Proximity to wells enables strong convective heat transfer and elevated fluid velocities within this region, which functions as the primary pathway for injected heat to reach production wells.

The peripheral zone maintains lower temperatures, exhibiting a sharp thermal interface with the inner convective core. Located distantly from injection/production wells with minimal fluid flow, temperature elevation here depends predominantly on conductive heat transfer. Consequently, the formation partitions into convective and peripheral zones, constituting the dual-zone thermal configuration illustrated in Fig. 19.

The dual-zone thermal configuration comprises two distinct regions: the convective zone and the peripheral zone. The convective zone serves as the primary pathway for fluid movement between injection and production wells, while simultaneously functioning as an efficient thermal storage reservoir and equilibration system for multi-energy complementarity in aquifers. In contrast, the peripheral zone maintains formation-equilibrium temperatures with minimal fluid flow, establishing a sharp thermal interface between the two zones.

During initial injection, thermal energy enters the formation via the injection well, displacing native formation water toward the production well. As the production well initially yields this native water, its temperature aligns with ambient formation conditions. Formation temperatures rise as thermally equilibrated flow reaches the production well, triggering rapid temperature escalation in production fluids – herein defined as the rapid heating stage. Throughout this phase, injected thermal energy is predominantly absorbed by convective zone rocks.

Subsequently, diminishing temperature differentials between the convective zone and injected fluid reduce thermal absorption capacity, initiating the slow heating phase. Upon thermal equilibration between injection fluid and convective zone, production temperatures stabilize (Fig. 8). Crucially, even during this stable stage (Stage D), production temperatures exhibit gradual ascent. This occurs because thermal energy continually dissipates outward from the convective zone through conduction rather than convection. Reduced external heat dissipation

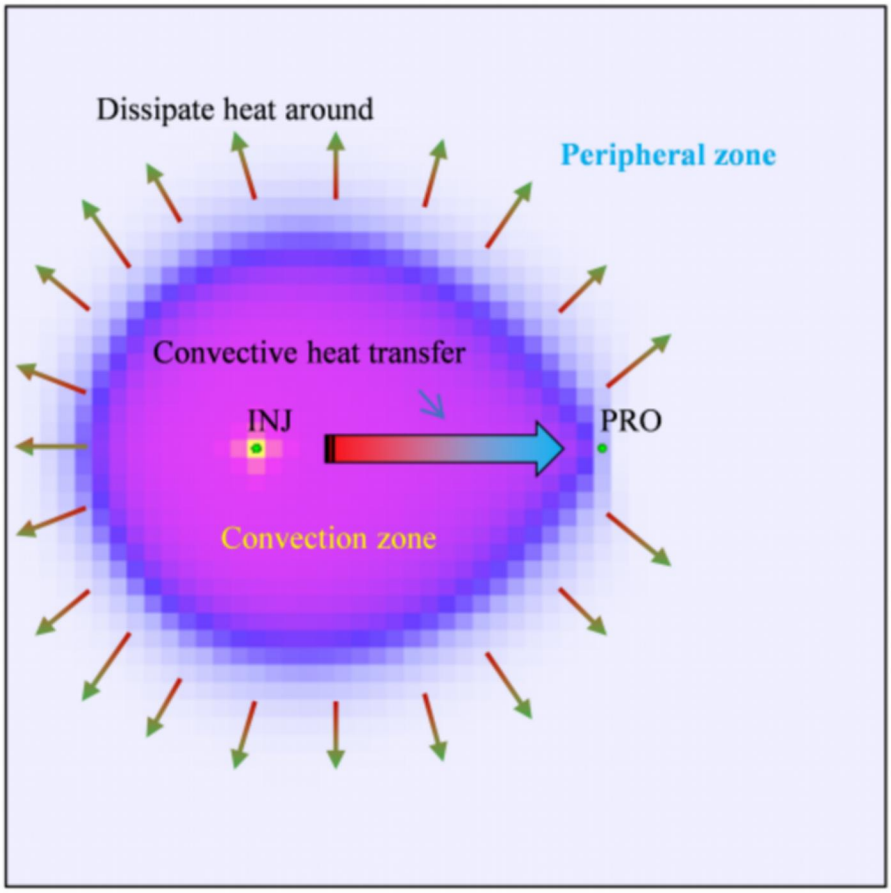

Fig. 19 The dual-zone thermal configuration of formation

from the convective zone enables progressive temperature elevation in production fluids.

The dual-zone configuration necessitates convective heat transfer as the predominant thermal mechanism. Within the convective zone, convective processes dominate thermal evolution while conductive effects are negligible. Conversely, the peripheral zone exhibits minimal flow velocities, rendering convective heat transfer insignificant; thermal conduction thus governs heat transfer exclusively. A marked thermal contrast exists: the convective zone sustains elevated temperatures while the peripheral zone maintains lower thermal regimes. Consequently, regulating conductive heat flux from the convective to peripheral zones emerges as the critical determinant of system heat loss. Therefore, subsequent research must prioritize quantifying convective zone thermal geometry and investigating parameters regulating inter-zone conductive transfer.

The formation's thermal conductivity critically governs heat transfer efficiency, necessitating optimal thermal insulation performance. This requires low thermal conductivity in reservoir rocks and overlying/underlying caprocks. This is not the same as the conventional geothermal extraction demand. In standard geothermal systems, the convective zone maintains lower temperatures than the peripheral zone, requiring heat conduction from surrounding formations to elevate fluid temperatures. Consequently, conventional geothermal development prioritizes formations with enhanced thermal conductivity. The dual-zone thermal configuration elucidates core distinctions between thermal energy storage and geothermal extraction systems: whereas geothermal systems necessitate convective zone heat absorption from peripheral regions, thermal storage systems require maximal heat retention within the convective zone.

7 Discussion and limitation

7.1 Advantages of the system

Against the backdrop of carbon neutrality, various methods currently exist for storing and balancing wind and solar power, including technologies such as pumped hydro storage, underground cavern storage, hydrogen electrolysis, and batteries. While these methods possess certain advantages and have reached a certain level of maturity, they primarily involve surface or shallow storage and face challenges such as battery risks (fire, pollution from waste), land use issues, and safety concerns related to underground engineering. The geothermal aquifer energy storage method proposed here utilizes geothermal reservoirs themselves, integrating directly with geothermal development. This approach transforms the traditional geothermal system from functioning merely as a "battery" (only discharging heat) into a "power bank" role (capable of both storing and discharging heat). Furthermore, unlike traditional Aquifer

Thermal Energy Storage (ATES), which primarily relies on the heat storage capacity of the formation, the new system mainly leverages the temperature balancing function of the geological formation. Therefore, although this system is based on the conventional ATES framework, it represents a novel application model that extends its fundamental principles. This new mode expands the application scenario for deep geological strata in storing wind and solar energy.

7.2 How to rapidly realize system utilization

A key concern for investors is the time-to-effect of the system. Achieving early results can shorten the investment cycle. The essence of this issue lies in the response time. As shown in Table 2, the response time advances with an increase in pressure differential and permeability, while it slightly delays with an increase in porosity and volumetric heat capacity. In contrast, injection temperature and rock thermal conductivity have no significant impact on the response time. In summary, the key factor influencing the time-to-effect is the reservoir's flow characteristics: the faster the fluid flows within the aquifer, the earlier the system takes effect.

The above analysis provides two approaches for shortening the time-to-effect. The first relates to site selection. Sites should preferably feature aquifers with high permeability. It is worth noting that permeability is generally correlated with porosity; highly permeable aquifers also tend to have higher porosity. Although increased porosity may slightly delay the response time, its impact is relatively minor. Compared to the advantages brought by enhanced permeability, the delay caused by porosity is negligible. The second approach involves the production strategy. During injection, appropriately increasing the injection-production pressure differential can enhance flow rate and shorten the time-to-effect.

7.3 How to ensure stable system operation

Section 6.3 introduced a dual-zone configuration. Based on the understanding of this mechanism, when the average temperature of the injected fluid is higher than the initial temperature of the aquifer, heat from the convection zone transfers to the peripheral zone via thermal conduction, resulting in increased heat loss (as validated in Section 5.1). Conversely, if the average temperature of the injected fluid is lower than that of the peripheral zone, heat from the peripheral zone supplements the convection zone, thereby utilizing the formation's thermal energy. However, lower injection fluid temperatures complicate subsequent utilization. Ideally, the formation temperature should remain stable, with no heat dissipation to the formation or absorption of energy from it. This is achieved when the injection temperature matches the formation temperature. Under this condition, the geothermal reservoir faces no service-life limitation, thereby resolving the challenge of long-term stable system operation.

7.4 Discussion on heat extraction efficiency

Existing research has identified multiple energy storage modes, including pumped hydro storage, compressed air energy storage, flywheel energy storage, electrochemical storage, hydrogen storage, and heat storage (Liu et al., 2025; Yan, 2023; Niu et al., 2023). The energy utilization efficiency and key characteristics of these different storage modes are summarized in Table 3. It should be noted that the heat storage referred to in this table mainly denotes above-ground thermal energy storage. Overall, the energy utilization rates of these different storage methods vary widely, influenced by factors such as storage duration and scale.

In this study, heat loss is specifically analyzed. By utilizing the intrinsic heat generation and storage mechanisms of the geothermal system, the loss of injected energy within the aquifer can be minimized. Results in section 5 indicate that the heat loss ranges from 2.8% to 11%, which is considered acceptable compared to conventional thermal loss levels. It should be clarified that the wellbore heat loss was not considered in the simulations performed in this study. However, our previous research on hot dry rock systems [28] has analyzed wellbore heat loss, demonstrating that it plays a critical role in the overall energy efficiency of geothermal development. Therefore, controlling wellbore heat loss is key to managing the total heat loss in the proposed system. It is an important aspect to address in future work.

7.5 Limitation

We construct a multi-energy complementary system based on aquifer geothermal energy, which can effectively convert unstable energy sources such as wind, solar, and industrial waste heat into stable energy output. However, due to the scope of our expertise, the study focuses primarily on the formation temperature characteristics within the energy balance module, while the other two modules receive less discussion. For instance, the energy collection module does not explore methods for achieving an optimal energy harvesting scheme, nor does the energy utilization module discuss how to improve the power generation efficiency of the dual-medium power generation system.

Furthermore, no quantitative evaluation is provided regarding the utilization efficiency. Issues such as wellbore heat loss and the conversion efficiency from thermal to electrical energy need to be considered in the context of efficiency. However, these limitations do not invalidate the novel multi-energy complementary utilization model proposed in this study. This paper introduces a new conceptual approach, and the question of how to improve energy utilization efficiency can be addressed in future research. In fact, efficiency challenges also exist in other forms of energy utilization, such as wellbore heat loss in geothermal development and conversion efficiency in geothermal power generation.

8 Conclusions

This study establishes a multi-energy complementary system based on Aquifer Thermal Energy Storage (ATES). Hydrothermal coupling simulations were conducted within this system framework, followed by comprehensive sensitivity analyses of key parameters derived from numerical results. The principal conclusions are summarized as follows:

1. Aquifer thermal energy storage (ATES) systems achieve balanced energy conversion and stable output by injecting in-

Tab. 3 Energy efficiency, advantages, and disadvantages of various energy storage methods

Energy storage methods	Energy utilization efficiency	Advantages	Disadvantages
Pumped hydro storage	65–85%[26]	Mature technology, large capacity, long lifespan	Site-specific, long construction time, high initial cost
Compressed air energy storage	40–55%[24–27]	Mature technology, large scale, long lifespan	Geographically constrained
Flywheel energy storage	85–90%[24–25]	High power & energy conversion efficiency	Short discharge duration, low energy density
Electrochemical storage	60–90%[24–27]	Abundant & recyclable materials	Limited cycle life, fire safety concerns
Hydrogen storage	30–50%[24]	Cross-seasonal storage, versatile hydrogen applications	Low round-trip efficiency, high infrastructure & transport costs
Heat storage	80–95%[24]	High capacity, low cost, long storage duration	Low electrical-thermal-electrical efficiency

termittent renewable energy as thermal fluids, enabling multi-energy complementarity within aquifer formations.

2. Thermal attenuation of injected heat primarily results from conductive dissipation to surrounding formations and thermal equilibration (formation heating and heat absorption). The residual energy reaching production wells determines production temperature. Elevated injection temperatures, increased pressure differentials, enhanced permeability, and reduced rock thermal conductivity collectively elevate production temperatures, whereas volumetric heat capacity (VHC) and porosity exert marginal influence. System response time is predominantly controlled by fluid flow velocity, accelerated under high-permeability and elevated pressure-difference conditions.

3. In multi-energy complementary systems, convective and conductive heat transfer govern formation and production temperatures, with convective heat transfer constituting the dominant mechanism. Seepage parameters (pressure differential and permeability) demonstrate the most significant impact on production temperatures, followed by thermal conductivity coefficients; porosity and volumetric heat capacity (VHC) exhibit secondary influence.

4. Multi-energy complementary systems adopt a dual-zone thermal configuration (convection zone and periphery zone). Reducing formation thermal conductivity enhances thermal insulation performance, suppressing heat transfer to peripheral regions and decreasing system heat loss rates. This configuration provides a theoretical framework for optimizing geothermal extraction and related multi-energy systems.

Acknowledgements

This research was funded by National Natural Science Foundation of China (U25A20349),Hebei Natural Science Foundation (E2025210180) and the Science and Technology Project of Hebei Education Department (BJ2025142).

Data Availability

Data available on request from the authors.

Conflict of interest

The authors declare no competing interest.

References

Bloemendal M, Hartog N. 2018. Analysis of the impact of storage conditions on the thermal recovery efficiency of low-temperature ATES systems. *Geothermics*, **71**: 306–319. doi:10.1016/j.geothermics.2017.10.009.

Brown CS, Kolo I, Lyden A, et al. 2024. Assessing the technical potential for underground thermal energy storage in the UK. *Renewable and Sustainable Energy Reviews*, **199**: 114545. doi:10.1016/j.rser.2024.114545.

Bu XB, Jiang KQ, Guo ZP. 2022. Storing high temperature solar thermal energy in shallow depth artificial reservoir for space heating. *Scientific Reports*, **12**:19549. doi:10.1038/s41598-022-24003-0.

Computer Modelling Group Ltd. 2014. STARS User Guide: Advanced Process & Thermal Reservoir Simulator. Calgary, Alberta Canada.

Dahash A, Ochs F, Janetti MB, et al. 2019. Advances in seasonal thermal energy storage for solar district heating applications: A critical review on large-scale hot-water tank and pit thermal energy storage systems. *Applied Energy*, **239**: 296–315. doi:10.1016/j.apenergy.2019.01.189.

Els RDV, Stijn B, Niels H, et al. 2021. Towards Sustainable Heat Supply with Decentralized Multi-Energy Systems by Integration of Subsurface Seasonal Heat Storage. *Energies*, **14**(23): 7958–7958. doi:10.3390/en14237958.

Gao LH, Zhao J, An QS, et al. 2019. Thermal performance of medium-to-high-temperature aquifer thermal energy storage systems. *Applied Thermal Engineering*, **146**: 898–909. doi:10.1016/j.applthermaleng.2018.09.104.

Ghaebi H, Bahadori MN, Saidi MH. 2014. Performance analysis and parametric study of thermal energy storage in an aquifer coupled with a heat pump and solar collectors, for a residential complex in Tehran, Iran. *Applied Thermal Engineering*, **62**: 156–170. doi:10.1016/j.applthermaleng.2013.09.037.

Guo CB, Li C, Zhang KN, et al. 2021. The promise and challenges of utility-scale compressed air energy storage in aquifers. *Applied Energy*, **286**: 116513. doi:10.1016/j.apenergy.2021.116513.

Han BW, Wang SH, Zhang Z, et al. 2024. Numerical simulation

of geothermal reservoir thermal recovery of heterogeneous discrete fracture network-rock matrix system. *Energy*, **305**: 132306. doi:10.1016/j.energy.2024.132306.

Heldt S, Wang B, Hu LW, et al. 2021. Numerical investigation of a high temperature heat injection test. *Journal of Hydrology*, **597**: 126229. doi:10.1016/j.jhydrol.2021.126229.

Heldt S, Beyer C, Bauer S. 2024. Uncertainty assessment of thermal recovery and subsurface temperature changes induced by high-temperature aquifer thermal energy storage (HT-ATES): A case study. *Geothermics*, **122**: 103086. doi:10.1016/j.geothermics.2024.103086.

Huang YH, Pang ZH, Kong YL, et al. 2021. Assessment of the high-temperature aquifer thermal energy storage (HT-ATES) potential in naturally fractured geothermal reservoirs with a stochastic discrete fracture network model. *Journal of Hydrology*, **603**: 127188. doi:10.1016/j.jhydrol.2021.127188.

Kastner O, Norden B, Klapperer S, et al. 2017. Thermal solar energy storage in Jurassic aquifers in Northeastern Germany: A simulation study. *Renewable Energy*, **104**: 290–306. doi:10.1016/j.renene.2016.12.003.

Liu X, Li W, Guo X, et al. 2025. Advancements in Energy-Storage Technologies: A Review of Current Developments and Applications. *Sustainability*, **17**(18): 8316–8316. doi:10.3390/su17188316.

Mantei N, Rioseco EM, Moeck IS. 2025. Parametric analysis of geothermal reservoir performance in Mesozoic sandstone formations within the North German Basin developed by multi-well systems. *Geothermal Energy*,**13**(1): 26. doi:10.1186/s40517-025-00349-2.

Niu QH, Ma KY, Wang W, et al. 2023. Multifactor analysis of heat extraction performance of coaxial heat exchanger applied to hot dry rock resources exploration: A case study in matouying uplift, Tangshan, China. *Energy*, **282**: 128277. doi:10.1016/j.energy.2023.128277.

Novo AV, Bayon JR, Castro-Fresno D, et al. 2010. Review of seasonal heat storage in large basins: Water tanks and gravel–water pits. *Applied Energy*, **87**: 390–397. doi:10.1016/j.apenergy.2009.06.033.

Pellegrini M, Bloemendal M, Hoekstra N, et al. 2019. Low carbon heating and cooling by combining various technologies with Aquifer Thermal Energy Storage. *Science of the Total Environment*, **665**: 1–10. doi:10.1016/j.scitotenv.2019.01.135.

Perera A.T.D., Soga Kenichi, Xu Yujie, et al. 2023. Enhancing flexibility for climate change using seasonal energy storage (aquifer thermal energy storage) in distributed energy systems. *Applied Energy*, **340**: 120957. doi:10.1016/j.apenergy.2023.120957.

Ren DW, Hou JM, Xiao JY, et al. 2021. Exploration of Key Technologies for Energy Storage in the Cleansing Transformation of Energy and Power. *High Voltage Engineering*, **47**(08): 2751–2759. doi:10.13336/j.1003-6520.hve.20201056.

Roded R, Aharonov E, Szymczak P, et al. 2024. Solutions and case studies for thermally driven reactive transport and porosity evolution in geothermal systems (reactive Lauwerier problem). *Hydrology and Earth System Sciences*, **28**(20): 4559–4576. doi:10.5194/hess-28-4559-2024.

Wang JC, Tan XF, Zhao ZH, et al. 2024. Coupled thermo-hydro-mechanical modeling on geothermal doublet subject to seasonal exploitation and storage. *Energy*, **293**: 130650. doi:10.1016/j.energy.2024.130650.

Yan WX. 2023. Research on Method of Constructing New Aquifer Thermal Energy Storage System to Absorb Large Capacity New Energy. Chongqing University.

Zhang W, Wu CD, Liu SB, et al. 2024. Characteristics and genesis of geothermal systems in the southern Junggar Foreland Basin, NW China. *Journal of Asian Earth Sciences*, **276**: 106363. doi:10.1016/j.jseaes.2024.106363.

Zhang YY, Gao XR, Sun CX, et al. 2024. Thermal performance and analysis of high-temperature aquifer thermal energy storage based on a practical project. *Journal of Energy Storage*, **82**: 110399. doi:10.1016/j.est.2023.110399.

Zhou DJ, Li K, Gao HH, et al. 2024. CO_2 high-temperature aquifer thermal energy storage (CO_2 HT-ATES) feasible study: Combing the heating storage and CCUS. *Gas Science and Engineering*, **122**: 205224. doi:10.1016/j.jgsce.2024.205224.